3rd Workshop and 1st Challenge on Data Assimilation & CFD Processing for PIV and Lagrangian Particle Tracking

Book of Abstracts

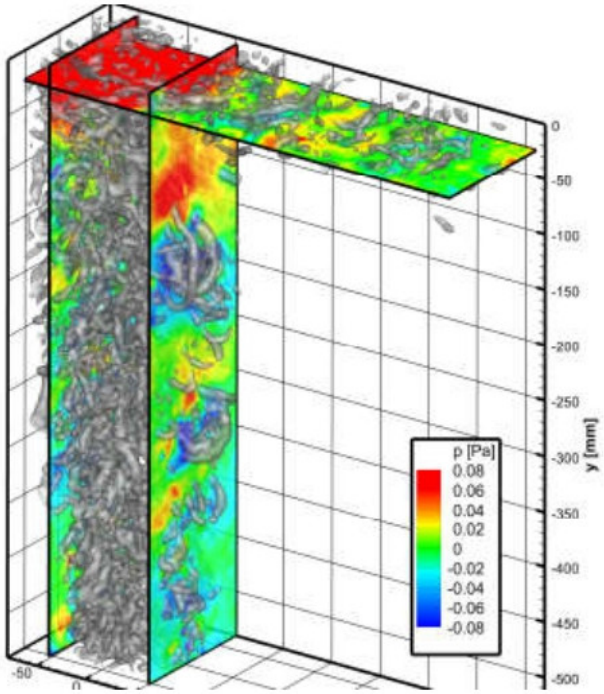

Online workshop on Thursday-Friday, November 19-20, 2020

HOMER

HORIZON 2020

DLR ONERA THE FRENCH AEROSPACE LAB TU Delft

3rd Workshop and 1st Challenge on Data Assimilation & CFD Processing for PIV and Lagrangian Particle Tracking, Online-Workshop, November 19 -20, 2020

Preface

This 3rd workshop on “CFDforPIV” has been jointly organized by DLR, ONERA and TU Delft in the frame of the H2020 project HOMER (GA number 769237) and follows the tradition of the two previous workshops organized 2016 in Lisbon and 2017 in Delft. It comprises of contributions from developers who are aiming at improving image processing methods for time-resolved and/or 3D Particle Image Velocimetry (PIV) or Lagrangian Particle Tracking (LPT) or enhancing the information measured by using techniques imported from the CFD and applied mathematics community. The advent of time-resolved and volumetric measurements has multiplied the possibilities with much excitement of the PIV and LPT community as well as of researchers in the field of applied fluid mechanics. The methods range from regularization strategies using the (simplified) Navier-Stokes-equation or the use of the momentum equation to obtain pressure from velocity and acceleration measurements, over machine learning approaches to variational data-assimilation frameworks using adjoint CFD.
In the frame of the 1st Challenge on Data Assimilation and Lagrangian Particle Tracking a synthetic experimental procedure generating virtual particle trajectories and camera images has been developed allowing for testing and assessing the capabilities of LPT evaluation codes and data assimilation approaches. A direct comparison of results gained with different existing and new codes became possible while each result can be assessed individually with the given ground truth input data based on a LES simulation of a complex turbulent shear flow and related uncertainty measures can be delivered.
This Book of Abstracts shall summarize the research presented at the 3rd workshop on “CFDforPIV”. Hopefully the event will spark new ideas and collaborations!

Benjamin Leclaire
Andrea Sciacchitano
Andreas Schröder
November 2020, Paris, Delft, Göttingen

3rd Workshop and 1st Challenge on Data Assimilation & CFD Processing for PIV and Lagrangian Particle Tracking, Online-Workshop, November 19 -20, 2020

Final Program

Time slot	First author	Communication title
Thursday, Nov 19th		
8:45-9:00	Organizers	Welcome and introduction
9:00-9:25	Manovski, P.	Velocity and pressure measurements of a turbulent boundary Layer at 80 kHz using 2D PIV
9:25-9:50	Schanz, D.	Shake-The-Box particle tracking with variable time-steps in flows with high velocity range (VT-STB)
9:50-10:15	Giannopoulos, A.	A dense PIV system: a solution for rapid data assimilation
10:15-10:30		Break
10:30-10:55	Cortina-Fernandez, J.	Data-enhanced particle tracking velocimetry
10:55-11:20	Yang, Y.	Kernelized LPT and Lagrangian PIV
11:20-11:55	Rahimi Khojasteh, A.	Lagrangian Coherent Track Initialisation
11:55-13:30		Lunch break
13:30-13:55	Kim, D.	AI-based data assimilation: sound level spectra from time-resolved 3D LPT
13:55-14:20	He, C.	Sequential data assimilation for unsteady flow pressure determination using continuous adjoint formulation
14:20-14:45	Zauner, M.	Nudging the Reynolds-Averaged Navier-Stokes equations with synthetic PTV-data of the square cylinder flow at Re=22 000
14:45-15:00		Break
15:00-15:25	Jeon, Y.J.	Eulerian time-marching in Vortex-In-Cell method by optimizing 4D boundary conditions
15:25-15:50	Scarano, F.	Velocity field reconstruction with time segment assimilation
15:50-16:20	Gesemann, S.	FlowFit3: Fast Data Assimilation for Recovering Instantaneous Details of Incompressible Flows based on scattered data
Time slot	**First author**	**Communication title**
Friday, Nov 20th		
9:00-9:25	Suzuki, T.	Development toward PSP-driven CFD simulation
9:25-9:50	Saredi, E.	State observer data assimilation for RANS with time-averaged 3D-PIV data
9:50-10:15	Mons, V.	Enhanced mean flow reconstruction from punctual measurements through optimal sensor placement
10:15-10:30		Break
1st Challenge on LPT and DA		**Communication title**
10:30-11:00	Leclaire, B.	Challenge datasets generation: physical situation, numerical simulation and synthetic generation
11:00-12:00	Sciacchitano, A.	LPT Challenge results
12:00-13:30		Lunch break
13:30-14:15	Sciacchitano, A.	DA Challenge results
14:15-15:00	Organizers + participants	Conclusions, discussions and way forward

3rd Workshop and 1st Challenge on Data Assimilation & CFD Processing for PIV and Lagrangian Particle Tracking, Online-Workshop, November 19 -20, 2020

3rd Workshop and Challenge on Data Assimilation & CFD Processing for PIV and LPT
November 19-20, 2020, virtual online meeting

Velocity and pressure measurements of a turbulent boundary Layer at 80 kHz using 2D PIV

Peter Manovski[1,2], Paul Gulotta[1,3], Matteo Giacobello[1], Charitha de Silva[4], Nicholas Hutchins[2] and Ivan Marusic[2]
[1]Aerospace Division, Defence Science and Technology Group, Melbourne, Australia
Peter.Manovski@dst.defence.gov.au
[2]Mechanical Engineering, University of Melbourne, Melbourne, Australia
[3]Air Force Research Laboratory, United States Airforce, USA
[4]School of Mechanical and Manufacturing Engineering, University of New South Wales, Sydney, Australia

Abstract

High-speed particle image velocimetry (PIV) was used to measure the turbulent boundary layer over a body of revolution. A narrow wall-normal strip of the flow field was captured using a high-speed laser and camera at a recording frequency of 80 kHz. The resulting high-speed PIV statistical quantities were shown to compare well with dual-pulse high-resolution PIV and direct numerical simulations (DNS), at similar conditions. The high-speed PIV velocity energy spectra were found to compare well with hot-wire spectra. The instantaneous pressure field was indirectly extracted by methods outlined in [1]. Preliminary pressure fields from PIV are presented and will be subject of further investigation.

The measurements were conducted at the Defence Science and Technology (DST) Group Low Speed Wind Tunnel. The test section is an irregular octagon, 2.74 m wide, 2.13 m high, and 6.56 m long. The geometry used in this study is an axisymmetric body of revolution and is based on a concept design of a conventional diesel-electric submarine without a casing or appendages. Such geometries are of particular interest in the maritime and aeronautical domains as they represent the simplest form of an underwater craft or aircraft fuselage and thus serve as an excellent benchmark to assess near-wall flow quantities before embarking on more complex geometries. The test model, as mounted on twin airfoil supports is shown in Fig. 1(b) and has length (L) of 2000 mm, and a diameter (D) of 273.66 mm. Refer to [3] for a detailed description of the model. The model was tested at zero incidence (yaw and pitch) with a tunnel airspeed of 28.8 m/s. The nominal Reynolds number based on the length of the model, $Re_L = 4.0 \times 10^6$. A circumferential ring of trip dots was located on the nose at 5%L to enable laminar-to-turbulent transition of the surface flow. The high-speed PIV measurements were conducted at the axial stations (x/L) indicated in Fig. 1(a).

Two-dimensional (2D) PIV was undertaken with tracer particles (DEHS) illuminated by an InnoLas Nanio Air (532-10-V-SP) high-speed laser and imaged by a Phantom v2640 high-speed camera. The displacement of particles in interrogation windows (IW) was determined by LaVision DaVis 10.1 PIV software. The laser light sheet was aligned with the stream-wise direction with the camera orthogonal to the laser sheet therefore allowing the measurement of instantaneous streamwise (U) and wall-normal (W) velocity components. The high-speed PIV method outlined by [4] is employed. The light sheet of the high-speed laser is limited to a narrow strip (5 mm × 55 mm), in the stream-wise and wall-normal directions, to maintain sufficient laser energy for PIV. An image magnification of 24.62 px/mm was achieved by using a large focal length lens, Nikon AF-S 400 mm f2.8 lens with an actuated aperture control mechanism as described in [3]. For a capture rate of 80 kHz, camera limitations required a cropped image width in the x-direction of 144 px and 1664 px in the z-direction. The camera on-board RAM (288 GB) allowed 800,000 consecutive images to be collected over 10 s. The high-speed PIV measurements were compared with two-pulse high-resolution 2D PIV measurements which were obtained with a Nikon AF-S 300 mm f4 lens fitted with a 3× teleconverter. At an observation distance of 1.5 m, the spatial resolution for the high-resolution PIV was 121.2 px/mm. For both PIV methods, elliptical 4:1 aspect ratio Gaussian weighted IW are employed with the larger dimension in the flow direction to maximise wall-normal spatial resolution while ensuring sufficient particle counts per sample.

The focus of this paper will be at the axial station $x/L = 0.449$. At this location the boundary layer flow exhibits a near zero pressure gradient - ZPG (-0.4 Pa/m). Since the curvature parameter (defined as the ratio of the boundary layer thickness, $\delta_{99} = 13.39$ mm, to the radius of curvature, $r_m = 133.9$ mm) is small (i.e. $\delta_{99}/\mathrm{r_m} \ll \mathrm{O}(1)$), the flow here, should follow the canonical flat plate solution [3]. The PIV measured boundary layer characteristics at $x/L = 0.449$ are as follows, the estimated friction velocity, $u_\tau = 1.17$ m/s (via Clauser chart), viscous length-scale, $\nu/u_\tau = 0.012$ mm (a `+' superscript indicates inner normalisation by u_τ/ν), the skin friction coefficient, $C_f = 0.00319$, and shape factor, $H = 1.40$. The corresponding momentum thickness Reynolds number, $Re_\theta = 3163$ and friction Reynolds number, $Re_\tau = 1087$. The measured boundary layer data are compared with canonical flat plate DNS [4]. The DNS parameters are, $C_f = 0.00312$, $H = 1.395$, $Re_\theta = 3270$ and $Re_\tau = 1040$, indicating only a small mismatch with our $x/L = 0.449$ data.

The boundary layer profiles and normalised Reynolds stresses for both PIV methods and DNS are shown in Fig. 1(c). The corresponding IW size in wall units (IW^+) for both the PIV methods are shown. Following the method of [2], the DNS data are filtered to match the spatial resolution of PIV (with x, y, z resolution: IW^+, light-sheet thickness$^+$, IW^+) and

are also plotted in Fig. 1 (c). The pre-multiplied power spectral densities (PSD) are shown in Fig. 1(d) for five wall heights and are compared with hot-wire measurements (at $z^+ = 100$ and 560). The hot-wire signal was acquired at 20 kHz but was truncated at 8 kHz due to spurious high frequency noise. For the high-speed PIV the cut-off frequencies based on the finite *IW* width (16 px = 0.65 mm) are shown at the two wall heights. The good agreement between the PIV, hot-wire and the DNS filtered data validates the accuracy of the PIV datasets.

The instantaneous pressure fields were extracted from the high-speed PIV velocity fields using DaVis 10.1 pressure solver [1], which integrates the pressure gradient of the incompressible Navier-Stokes equations. The material derivative term was obtained by pseudo-Lagrangian tracking of the PIV velocity fields, where a quadratic polynomial is fitted iteratively at each grid point to match the velocity fields over 5 time-steps. Velocity and acceleration at each grid point are then evaluated from the polynomial fit. The pressure field is obtained by numerically solving a Poisson equation. A space-time block size of 5 time-steps was simultaneously considered for a single solution to the Poisson equation. An additional step of estimating the convection velocity was performed to strengthen the temporal coherency. Neumann boundary conditions were used at each boundary and Dirichlet in the freestream, corresponding to the tunnel freestream static pressure (102.032 kPa). A preliminary instantaneous pressure field is shown in Fig. 1(e). Prior to conducting a detailed study, a series of comparisons will be undertaken to validate the extracted pressure from the high-speed 2D PIV. Firstly, the mean pressure at the nearest wall measurement point will be compared with the static wall pressure from [3]. Secondly, the mean pressure field will be compared with the boundary layer profile measured by a Pitot probe from [3]. Finally, the pressure fluctuations from the PIV will be compared with the DNS data of [4].

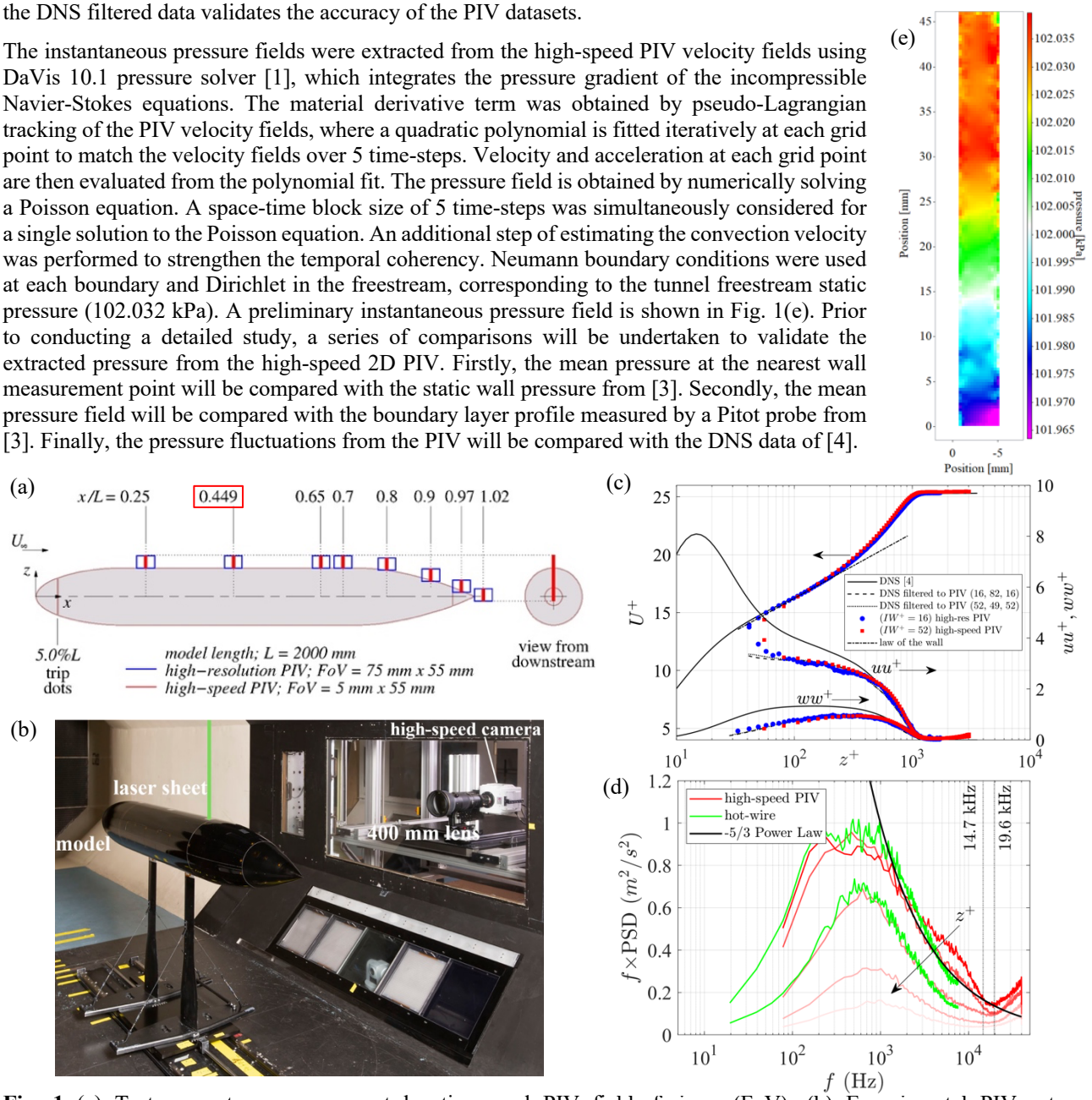

Fig. 1 (a) Test geometry, measurement locations and PIV field-of-views (FoV). (b) Experimental PIV set-up. At measurement station, $x/L = 0.449$, (c) boundary layer profiles (U^+) and normalised Reynolds stresses (uu^+, ww^+) from PIV compared with DNS [4], (d) pre-multiplied energy spectra ($f\times$PSD) at five wall-heights compared with hot-wire (at $z^+ = 100$ and 560), and (e) an instantaneous pressure field.

References

[1] Jeon Y.J., Müller M., Michaelis D., Pfeiffer K., Wieneke B. (2017) Boundary condition assignment for evaluating instantaneous pressure field from TR-PIV, 12th International Symposium on Particle Image Velocimetry, Busan, Korea

[2] Lee, J. H., Kevin, Monty, J. P., and Hutchins, N. (2016) Validating under-resolved turbulence intensities for PIV experiments in canonical wall-bounded turbulence. Experiments in Fluids, 57(8):129. doi: 10.1007/s00348-016-2209-6.

[3] Manovski, P., Jones, M. B., Henbest, S. M., Xue, Y., Giacobello, M. and de Silva, C. (2020) Boundary layer measurements over a body of revolution using long-distance particle image velocimetry. International Journal of Heat and Fluid Flow. 83, 108591. doi.org/10.1016/j.ijheatfluidflow.2020.108591

[4] Schlatter, P. and Örlü, R. (2010) Assessment of direct numerical simulation data of turbulent boundary layers, Journal of Fluid Mechanics. 659:116–126. doi:10.1017/S0022112010003113

[5] Willert, C. E. (2015) High-speed particle image velocimetry for the efficient measurement of turbulence statistics, Experiments in Fluids. 56(17). doi.org/10.1007/s00348-014-1892-4

3rd Workshop and Challenge on Data Assimilation & CFD Processing for PIV and LPT
November 19-20, 2020, virtual online meeting

Shake-The-Box particle tracking with variable time-steps in flows with high velocity range (VT-STB)

Daniel Schanz[1], Matteo Novara[2] and Andreas Schröder[1]
[1]Institute of Aerodynamics and Flow Technology, German Aerospace Center (DLR), Göttingen, Germany
daniel.schanz@dlr.de

Abstract
In recent years, Lagrangian Particle Tracking (LPT) has become more and more important in the field of 3D flow measurements, largely due to the introduction of the methods of Iterative Particle Reconstruction (IPR, Wieneke 2013) and Shake-The-Box (STB, Schanz et al. 2016). Applying the STB algorithm, particles can be tracked in large numbers, with a nearly complete suppression of ghost particles. The ability of the STB algorithm to discern real particles from ghost particles is largely stemming from the observation that for real particles the change of acceleration is small between time-steps, while ghost particles are generated in quasi-random locations all over the measurement volume. However, this assumption only holds if the particles exhibit a certain amount of movement relative to each other, such that the ambiguities 'de-correlate' within few time-steps. In many flows this assumption holds, however flows with a high velocity range can exhibit regions in space with only very little movement of the particles (e,g, jet flows). As the time separation has to be chosen such that the fastest particles are reliably tracked, particles in the surrounding flow might move only a fraction of a pixel in the same time. Another potentially problematic effect of slowly moving particle clouds is that situations of overlapping particle images are retained over several time-steps.
We see that a slowly moving particle field is detrimental to the tracking process in multiple ways. In this work we propose an extension to the standard STB evaluation, which applies multiple iterations of particle tracking with variable time-separation. The idea is to start the evaluation with a time separation such that the slowest particles of the flow can be optimally tracked. From there, the time-separation is iteratively reduced, tracking faster and faster particles with every iteration. Finally, the original time-separation of the recording is reached, where only the fastest particles - whose velocity initially determined the recording rate - remain to be tracked. The involved steps are detailed in the following

1. Choose a suitable temporal $\Delta_{s,i=1}$ such that the *slowest particles* move at least one particle image diameter from image to image, where $\Delta_{s,i=1}$ is the number of omitted snapshots.
2. Perform *particle tracking* on the selected subset of snapshots.
3. *Filter* the gained trajectories using a fitting method with a suitable kernel-size.
4. Choose a *finer temporal resolution* $\Delta_{s,i+1} < \Delta_{s,i}$ for the next iteration.
5. *Interpolate* the filtered trajectories from $\Delta_{s,i}$ to the time-steps given by $\Delta_{s,i+1}$
6. Perform *particle tracking* on the snapshots given by $\Delta_{s,i+1}$, while feeding the interpolated particle clouds from the previous iteration as a partial pre-solution to the reconstruction of each snapshot
7. Repeat steps from 3 to 6 until $\Delta_{s,i+N} = 1$ is reached.

The VT-STB approach is applied to an experimental dataset, measuring the flow of a small diameter jet impinging on a circular cylinder. The setup is placed in a regular cylindrical 16-faces glass tank (see Fig. 1). A jet is generated by a nozzle of diameter $d = 3$ mm and is impinging onto a circular cylinder with diameter $d_C = 52$ mm at an angle of 45°.

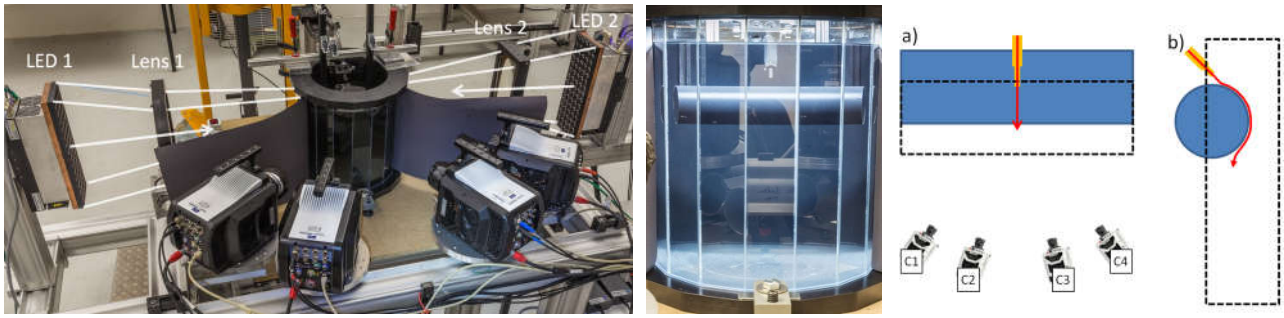

Fig. 1: Left: Setup for the water jet experiment. with four Phantom V2640 cameras viewing into the water tank, which is illuminated from two sides by high-power white LED arrays. Middle: 16-face water tank with submerged cylinder ($d_c = 52$ mm) and $d = 3$mm nozzle at 45° impinging angle. Right: Schematical experimental setup from top view (a), and side view (b). Cylinder in blue, nozzle in yellow, centerline flow in red and the illuminated area as a dashed line.

The maximum jet velocity was v_{MAX} = 6 m/s, corresponding to a Reynolds number of 17,875. For a more detailed description, see (Kim et al. 2018), where a comparable setup was employed in air.

VT-STB was applied in the following fashion: 5 iterations were performed, starting with a time separation of $\Delta_{s,1}$ = 79 time-steps (the slowest particle move approx. 2.4 pixel in this interval, corresponding to approx. one particle image diameter). The following iterations feature time separations of $\Delta_{s,i}$ = [36, 14, 6, 1] time-steps.

The operating principle of VT-STB is illustrated in Fig. 2, left. For each iteration, a 10mm - thick slice of the volume, centered around the nozzle is visualized, showing particle tracks over approx. 500 time-steps (based on the original sampling; the effective length varies slightly due to the different time separations). The particles tracked at $\Delta_{s,1}$ = 79 (see Fig. 2 left, top) are located in the entrainment region and below the cylinder, far from the wake of the jet. Maximum velocities of approx. 0.12 m/s are attained. When moving to iteration 3 ($\Delta_{s,3}$ = 14, Fig. 2 left, middle), maximum velocities of 0.7 m/s can be tracked. Large parts of the wake region below the cylinder appear in the tracking system. Finally, when $\Delta_{s,5}$ = 1 is reached in iteration 5 (Fig. 2 left, bottom), the remaining fast particles from the jet and its direct surroundings are tracked. Maximum velocities of 6 m/s are seen, as expected.

In order to assess the benefits of VT-STB over regular processing using Δ_s = 1, the results are compared to a normal STB evaluation over 1,000 images. Fig. 2 (right) shows comparisons between the two reconstructions in two selected subvolumes. Both evaluations correctly capture the vast majority of the tracks, however for STB a relevant amount of tracked particles appears within the cylinder, indicating ghost tracks (not shown here). For VT-STB this region is nearly completely void. When focusing on a smaller region (see Fig. 2, right, top) it is obvious that the normal STB-result is interspersed with both outliers, as well as a sizeable number of tracks with velocities close to zero, appearing in regions with visibly higher flow velocity. The VT-STB result is free of both types of abnormal particle tracks. At the same time, the tracks of slow particles exhibit less noise, as the filtering is carried out on a broader kernel, minimizing the effects of long-lasting overlap situations.

Similar pheneomena are seen when looking at a x-z plane located on the upper edge of the measurement volume, above the jet (viewing from top, see Fig. 2 right, bottom). The STB evaluation shows clear signs of 'line-of-sight'-tracks, where particles follow the viewing direction of a singular camera, as their intensity is mostly supported by a peak on that specific camera. Furthermore it can be seen that some of the particles in the center of the vortex that are present for VT-STB are missing for the STB evaluation.

For the examined flow, VT-STB processing shows profound advantages; however it has to be stressed that this case represents an extreme in terms of velocity range and volume ratio of fast and (very) slow moving particles. For most experimental investigations, normal STB evaluations will show significantly less ghost particles, still we expect benefits of VT-STB processing in many flows.

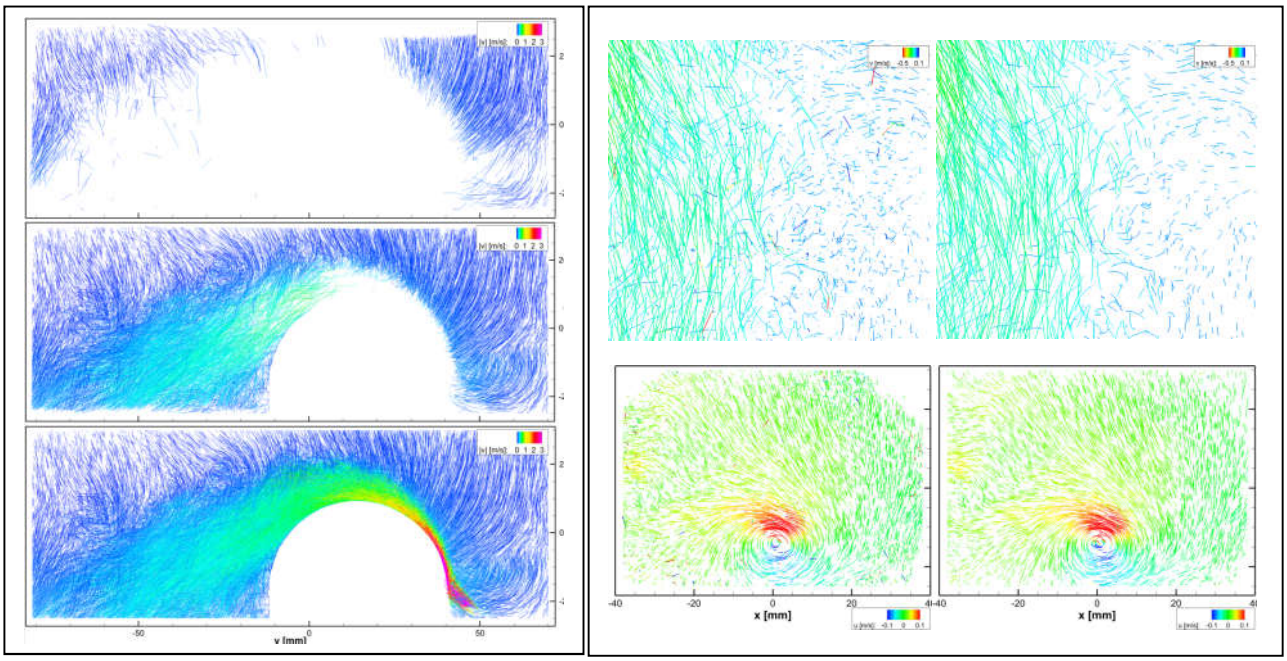

Fig. 2: Left: VT-STB tracking with 5 iterations, showing iterations 1, 3 and 5 with time separations of $\boldsymbol{\Delta_s}$ = 79, 14 and 1 time-steps. Right: STB processing (left) vs. VT-STB processing right) in two exemplary regions.

References

Kim, M., Kim, H. D., Yeom, E., & Kim, K. C. (2018). Flow characteristics of three-dimensional curved wall jets on a cylinder. Journal of Fluids Engineering, 140(4), 041201.

Schanz D, Gesemann S, Schröder A (2016) Shake-The-Box: Lagrangian particle tracking at high particle image densities. Exp Fluids 57(5), 70.

Wieneke B (2013) Iterative reconstruction of volumetric particle distribution. Meas Sci Technol 24:024008

3rd Workshop and Challenge on Data Assimilation & CFD Processing for PIV and LPT
November 19-20, 2020, Paris, France

A dense PIV system: a solution for rapid data assimilation

Antonios Giannopoulos[1,2], Pierre Chatelier[3] and Jean-Luc Aider[1]

Email: antonios.giannopoulos@espci.fr

[1] *Laboratoire de Physique et Mécanique des Milieux Hétérogènes (PMMH), CNRS UMR7636, ESPCI Paris, PSL Université, Sorbonne Université, Université Paris Diderot, Sorbonne Paris Cité, 75005 Paris, France*

[2] *Photon Lines, Parc Pereire Bat B, 99 rue Pereire, 78100 Saint-Germain-en-Laye, France*

[3] *See Fast Technologies,* 99 rue Péreire Parc Péreire, Bât.B, 78100 Saint-Germain-en-Laye

The presented system is developed around the image acquisition and processing platform Eyemotion, developed by SeeFast Technologies. Eyemotion is a native code software, with built-in image processing tools adapted for large data flows. It can be used for actuator signal sending and receiving, laser-camera synchronization and real-time image post-processing. We developed a plugin extension of the said software in a .NET platform, integrating a dense 2D-2C Lukas-Kanade Optical Flow (LKOF) PIV algorithm, implemented in CUDA functions. The algorithm was first developed at ONERA [1] and later adapted for the real-time calculation case by PMMH lab[2]. One vector per pixel is calculated, with a precision of the order of a tenth of a pixel and a maximum displacement of up to 20 pixels. The goal of the system is also the real-time calculation of other velocity-derived variables calculations, like vorticity field, λ_{ci} criterion and scalar values like the recirculation area, or the sum of the kinetic energy of the field. The system can be used in real-time mode, during image acquisition, or offline in post-processing mode. A continuous and pulsating laser mode was designed and integrated. A high and low calculation speed option can be selected for hardware and software parameters of the system, depending on the application. The only PIV parameters for the user are the kernel radius, the pyramid level size and the number of Gauss-Newton iterations [1]; no further complicated filters or spurious vector rejection process is applied.
The presented setup shows great potential in the fast PIV calculation, large data-base creation (suitable for data-hungry machine learning methods), and PIV setup diagnostic with relatively low disk space occupancy. The optimal setup consists of a high-speed camera, an optimal GPU, and a RAID0 disk configuration. Different versions of the system have been proven already to facilitate neural-network system identification experiments[3], as well as machine learning closed-loop control experiments[4]. The present LKOF algorithm has also be applied in different type of experiments, not only PIV images; an example of an application in a blood platelets flow experiment is presented in figure 3.

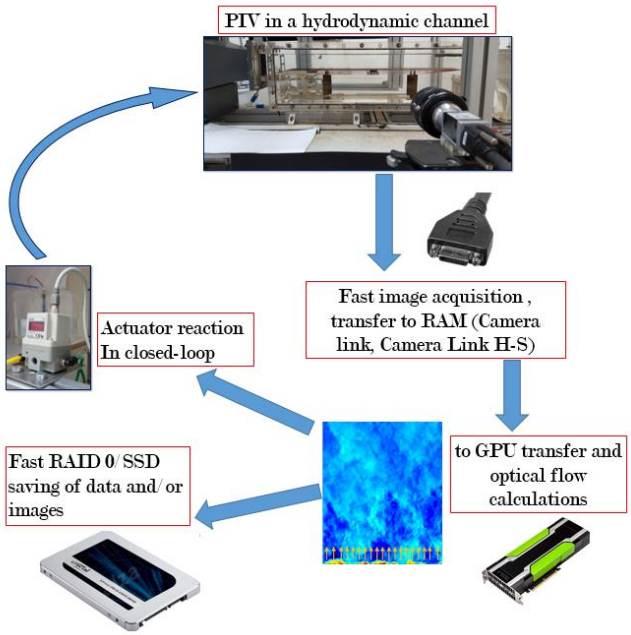

Fig. 1 System scheme: Optimized image acquisition, fields calculations, saving or actuator reaction.

The system spatial resolution and computational time has been validated using synthetic PIV images and various hydro/aerodynamic datasets (turbulent boundary layer, backward-facing step and grid turbulence wind tunnel experiments); it shows great potential for post-processing speed-up and saving in hard space. A real-time field saving option has been integrated, in order to avoid saving images and save disk space; fields are saved in a low disk space format. Particularly for 16 bit images, the value of Mb(field)/Mb(image) ratio is around 1, which shows that a saving of order 50% disk space can be achived. It has been tested for various image sizes up to 16 Mp and various GPUs. A multi-GPU calculation option is also being investigated.

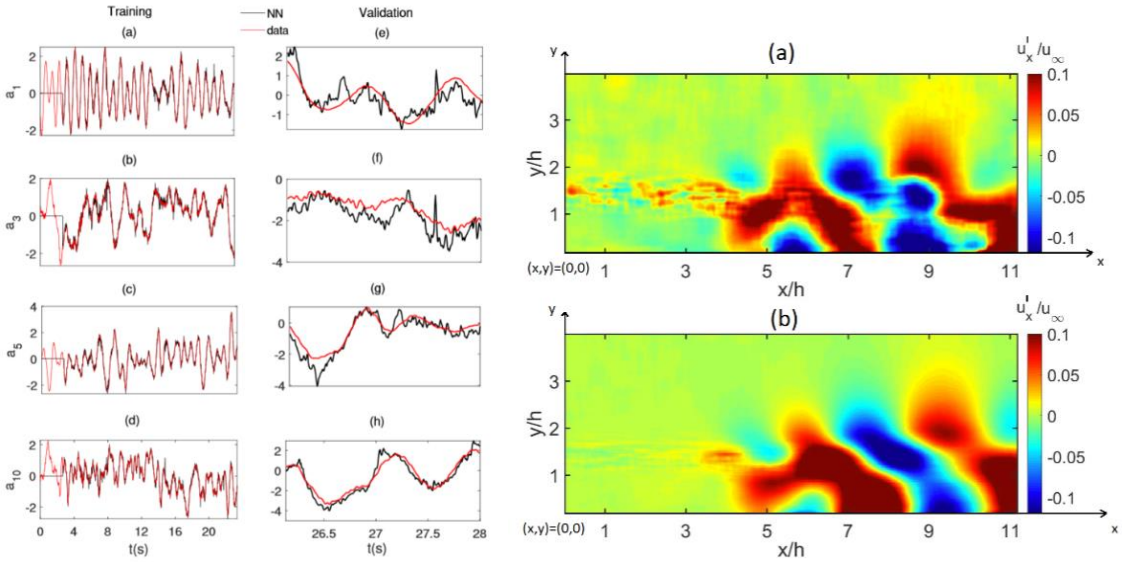

Fig. 2 POD coefficient prediction for neural-network training and validation dataset (left), and velocity field reconstruction (right) for experimental, time-resolved Backward Facing Step flow (Reh=1385).

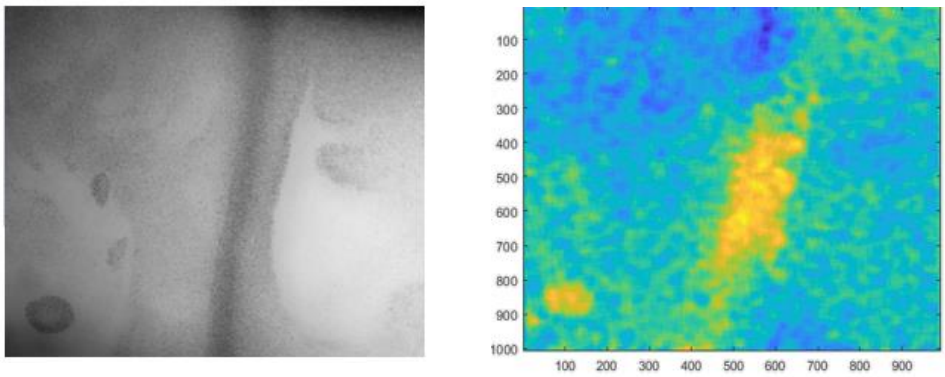

Fig. 3 Blood platelets flow image (left) velocity field calculation (right) Experiment from: L.Bellebon, PMMH.

References

[1] Champagnat et Al(2011) Fast and accurate PIV computation using highly parallel iterative correlation maximization Exp Fluids (2011) 50:1169–1182 ,DOI 10.1007/s00348-011-1054-x.

[2] Gautier, N. & Aider, J.-L., Real-time planar flow velocity field measurements using an optical flow algorithm implemented on GPU, Journal of Visualization, 1-10, 2014.

[3] A. Giannopoulos, J.-L. Aider, Prediction of the dynamics of a backward-facing step flow using focused time-delay neural networks and particle image velocimetry data-sets, International Journal of Heat and Fluid Flow, Volume 82, 2020, 108533, ISSN 0142-727X.

[4] N. Gautier, J.- L. Aider, T. Duriez, B. Noack, M. Segond, M. Abel Closed-loop separation using Machine Learning , J. Fluid. Mech, 770, 442 – 457 (2015).

3rd Workshop and Challenge on Data Assimilation & CFD Processing for PIV and LPT
November 19-20, 2020, virtual online meeting

Data-Enhanced Particle Tracking Velocimetry

Javier Cortina-Fernández[1], Carlos Sanmiguel Vila[1], Andrea Ianiro[1] and Stefano Discetti[1]
[1]Aerospace Engineering Research Group, Universidad Carlos III de Madrid, Leganés, Spain
sdiscett@ing.uc3m.es

Abstract

In recent years Lagrangian Particle Tracking (LPT) has received a renewed interest, fostered by the advances of volumetric velocimetry and technology for time-resolved applications. The main advantage of direct tracking of particle images resides in suppressing the averaging effect of cross-correlation-based algorithms. On the other hand, tracking of individual particles provides vectors/tracks on a scattered grid, thus posing the problem of interpolating data on a mesh for later data processing. In this process, the choice of the mesh size onto which interpolate the data is inevitably bound by the mean particle spacing. Considering that the particle spacing is spatially and temporally variable, often conservative selections should be pursued, unless temporal information or physical constraints are introduced. In non-time-resolved applications this is often hard to achieve, thus posing a limit to the final achievable resolution.

For statistical analysis, this limitation is overcome by Ensemble PTV (Cowen and Monismith 1997, Kähler et al. 2012), which is based on generating dense clouds of vectors from the ensemble of snapshots and averaging in bins with sufficiently large number of vectors to obtain local statistics. Enforcing ergodicity, it is possible to improve significantly the Dynamic Spatial Range of the statistics by blending information from the entire dataset. In principle the lower bound for the resolution relates directly to the root-mean-square error of the particle-center detection, thus resulting in a sub-pixel resolution limit (Kähler et al 2012). On the downside, however, the instantaneous information is dropped and in principle cannot be retrieved directly with the same resolution.

The Data-Enhanced Particle Tracking Velocimetry (DEPTV, Cortina-Fernández et al 2020) is an unsupervised model-free algorithm which merges the ideas of Ensemble PTV and of gappy Proper Orthogonal Decomposition (Everson & Sirovich 1995, Venturi & Karniadakis 2004) to create high-resolution *ensemble particle modes*. These modes constitute a fully data-driven dictionary for the extraction of high-resolution flow fields. The ensemble particle modes are obtained through the following procedure (the reader is referred to Cortina-Fernandez et al 2020 for a more complete description):

- PIV standard processing of the images, which will deliver the low-resolution velocity fields, to be arranged in the form of snapshot matrix (Sirovich 1987) U_{PIV} (with each row being a snapshot)
- Singular Value Decomposition of the snapshot matrix $U_{PIV} = \Psi_{PIV}\Sigma_{PIV}\Phi_{PIV}^{T}$
- PTV processing of the images to extract the scattered velocity vectors on each snapshot
- Selection of the bin size by setting the desired number of particles in each bin.
- Computation of the PTV snapshot matrix U_{PTV}, which contains, for each snapshot, 0 in empty bins and average velocity for bins containing one or more particles
- Calculation of high-resolution ensemble particle modes from projection of U_{PTV} on the PIV temporal basis Ψ_{PIV}, and scaling to account for the number of non-empty bins corresponding to each location:
$$(\Sigma\Phi^{\mathrm{T}})_{DEPTV} = \widehat{N} \odot \Psi_{PIV}^{T} U_{PTV}$$
where $\widehat{N}$ is the reciprocal of the fraction of non-empty bins for each location, and $\odot$ is the Hadamard product.
- Calculation of high-resolution velocity fields:
$$U_{HR} = \Psi_{PIV}(\Sigma\Phi^{\mathrm{T}})_{DEPTV}$$

The method is validated on numerical and experimental data. The experimental validation has been carried out in the Göttingen-type wind tunnel of UC3M, with test section of 40x40cm and turbulence intensity of 1%. Two side-by-side cylinders have been mounted in the test section, as illustrated in Fig. 1, left. The cylinders have diameter of D=20mm and d=2mm, respectively, and their axes separation is equal to D. Velocity field measurements are carried out in the wake of the cylinders using two ANDOR Zyla sCMOS 5.5MP cameras (2160x2560 pixel array, 6.5μm pixel size) with partially overlapped field of view. One camera is equipped with a Tokina objective with 50mm focal length, with resolution of approximately 10.3 pix/mm. This camera is used to test the DEPTV algorithm, since it would not have enough resolution to discretize the wake of the smallest cylinder. From now on it will be referred as “low-resolution”

camera. The other camera is equipped with a 100 mm focal-length Tokina objective, with a resolution of 22.6 pixels/mm, and will be used as a reference for comparison. This will be referred in the following as "reference" camera. The PIV image analysis was carried out with a multi-grid multi-pass code, with final interrogation window of 64x64 pixels for both cameras, and 75% overlap. A set of 12000 images is used for DEPTV to achieve sufficient convergence. The final bin size for DEPTV is 16x16 pixels, thus aiming to a x4 improvement of the dynamic spatial range.

An example of instantaneous crosswise velocity field obtained with the low-resolution and reference camera is reported in the first and second column of Fig.1, right. The freestream velocity U_∞ and the diameter of the larger cylinder D are used as reference quantities to represent the results in non-dimensional form. The center of the reference system corresponds to the axis of the larger cylinder. It can be observed that the standard PIV on the low-resolution cameras can capture the wake of the largest cylinder with reasonable accuracy if compared to the reference one. On the other hand, the vortices shed in the wake of the smallest cylinder are significantly attenuated. The results obtained with the DEPTV process are reported in the right column of Fig.1, right. It can be clearly observed that the wake features in the wake of the large cylinder are recovered with less smoothing than the standard PIV on the low-resolution camera, and that the fluctuations due to the vortices shed in the wake of the small cylinder are recovered. This is particularly evident when observing the inset of Fig.1, right, with a magnified view of the wake of the small cylinder.

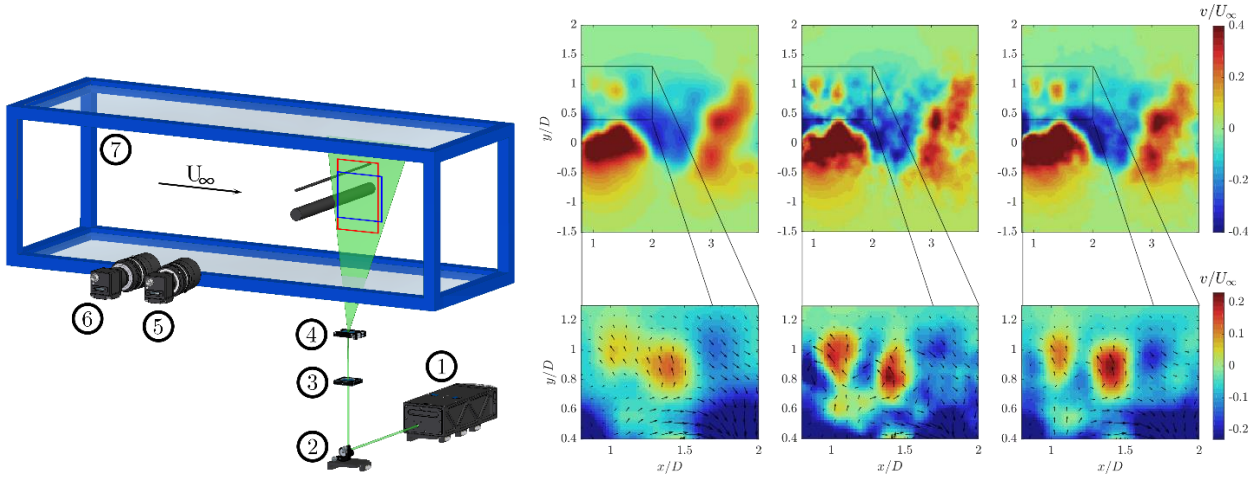

Fig. 1 Left: sketch of the experimental setup (1-laser, 2-mirror, 3-spherical lens, 4-cylindrical lens, 5-low-resolution camera, 6-reference camera, 7-wind-tunnel test section). The field of view of the low-resolution and reference cameras are indicated with a red and a blue rectangle, respectively. Right: comparison of the instantaneous crosswise velocity field for the low-resolution camera (left column), reference camera (center column) and DEPTV process on the low-resolution camera (right column). The top row includes the full field of view, while the inset is represented in magnified view in the bottom row. Figures adapted from Cortina et al. (2020).

Code availability

A sample Matlab code of the DEPTV algorithm is available on GitHub: https://github.com/StefanoDiscetti/DEPTV

Acknowledgements

CSV, SD and AI were partially supported by the Grant DPI2016-79401-R funded by the Spanish State Research Agency (SRA) and European Regional Development Fund (ERDF).

References

Cortina-Fernández J, Sanmiguel Vila C, Ianiro A, Discetti S (2020) From sparse data to high-resolution fields: ensemble particle modes as a basis for high-resolution flow characterization. Experimental Thermal and Fluid Science, 120:110178.

Cowen E, Monismith S (1997) A hybrid digital particle tracking velocimetry technique. Exp. Fluids, 22:199-211

Everson R, Sirovich L (1995) Karhunen-Loeve procedure for gappy data. J. Opt. Soc. Am. A, 12: 1657-1664.

Kähler CJ, Scharnowski S, Cierpka C (2012) On the resolution limit of digital particle image velocimetry. Exp Fluids, 52:1629-1639

Sirovich L (1987) Turbulence and the dynamics of coherent structures. II. Symmetries and transformations. Q. Appl. Math., 45:573-582

Venturi D, Karniadakis GE (2004) Gappy data and reconstruction procedures for flow past a cylinder. J. Fluid Mech., 519:315-336

3rd Workshop and Challenge on Data Assimilation & CFD Processing for PIV and LPT
November 19-20, 2020, virtual online meeting

Kernelized LPT and Lagrangian PIV

Yin YANG[1], Dominique HEITZ[1]
[1]INRAE, UR OPAALE, 35044 Rennes Cedex , France
yin.yang@inrae.fr

Abstract

Shake-the-Box (STB) method (Schanz er al. 2016) has become the *de facto* standard Lagrangian Particle Tracking (LPT) approach that reconstructs the 3D particle tracks from time-resolved particle-seeded stereoscopic images. To our knowledge, the STB is the only available LPT method on the market that works on highly concentrated particle images (beyond 0.1 particle per pixel (ppp)). Many developments on the STB method have been published ever since. Some developments concentrated on extending the power of STB to other types of data. For example, Novara et al. (2016, 2019) proposed the multi-pulse STB to deal with high-speed flow applications where the time-resolved data is not available. Tan et al. (2020) introduced the pruning algorithm to remove ghost particles and applied the STB method to blurred particle images. Others are more application-specific concerning a particular sub-module of the whole LPT workflow, such as the calibration procedure (Schröder et al., 2020). But very few works exist to improve the core tracking ability of STB. STB's core tracking scheme features a prediction phase that forecasts a particle's position for the current frame given its history and a correction phase that finds its optimal location around its predicted position by minimizing the gap between the records and the projected image residual. We argue that the optimization scheme in STB, initially proposed in Wieneke (2012), can be less effective or even fail with the sparse temporal data or with data extracted from complex flows. The consequences are either one track is terminated prematurely, or one particle is identified on the wrong track. The main reason is that STB's optimization scheme requires the cost function to be relatively smooth locally to perform well. This high level of smoothness can not be guaranteed when the predictor failed to provide a good starting point for data with large-time separation or local complicated flow structure. In this work, we propose a tracking scheme rooted in the function learning/approximation paradigm. For particle *p,* we intend to learn a nonlinear function **f** that maps the image set Π_p, containing the small square local patch I_p extracted from the recorded image for all cameras, to X_p, the particle's 3D coordinate. The function **f** can be learned by minimizing an empirical risk loss built on sample pairs (Π_p, X_p). The sample image set is obtained using the camera model and the optical transfer function. Under this formulation, the resulting algorithm can be solved efficiently using gradient-based algorithm therefore much more robust. This solution can be expressed efficiently using the kernel function $k(\bullet,\bullet)$. The kernel measures the similarities between the two sample images and controls the goodness of the solution. One is encouraged to choose a valid and pertinent kernel function that mostly represents the characteristic of data. Our approach is based on kernel methods and is thus called Kernalizaed LPT (KLPT). KLPT is evaluated against both synthetic and real experiments. The synthetic data is generated based on a Large Eddy Simulation data simulating the turbulent cylinder wake-flow at Re3900 (Parnaudeau et al. 2018). Figure 1 shows the mean error of detected particles of KLPT and compared to 2 different implementations of STB (one from an in-house code, one from the commercial software Davis10.4). Our KLPT produces satisfactory results for data with medium to high ppp levels and large time separation. We also apply KLPT and STB (Davis 10) to data depicting an impinging jet at Re2500. Figure 2 visualizes a subset of the tracks reconstructed by STB (left) and KLPT (right). We observe that, compared to STB, KLPT can capture longer tracks and allows more detailed flow reconstruction at highly turbulent regions. We conclude that our KLPT scheme always is more robust compared to STB and more accurate for densely seeded particle flow fields.

Another line of work concerning STB is to retrieve the volumetric data (typically velocity) on Eulerian grids from the Lagrangian data generated by STB. Representative methods include FlowFit (Gesemann et al. 2016) and VIC+ (Schneiders et al. 2016)/VIC# (Jeon et al. 2018). Their main idea is to leverage the volumetric velocity field between the particle-based data and an Eulerian dynamical model's solution. We argue that if only the Eulerian flow variables are needed, it is naturally more accurate to base our knowledge on raw images instead of passing through the redundant LPT procedure. On the other hand, the TomoPIV method estimates the volumetric velocity field by first reconstructing the 3D voxel intensity volume from 2D stereoscopic images, then inferring the 3D velocity vectors using volume

correlation techniques. Our proposed method Lagrangian PIV (LAPIV, Yang et al. 2019), differs from the above two approaches. Our primary motivation is to *directly* infer the volumetric velocity fields from raw image data without any intermediate procedure. To this end, we adopt the above kernel formulation under KLPT, taking account of a transport model that links the particles' 3D coordinate X at frame *k* to the Eulerian velocity field at frame *k-1*. By doing so, we are able to obtain the unknown flow velocity field. Our formulation allows estimating the velocity vector through tracking a group of particles, contrary to single-particle tracking done in KLPT. Naturally, LAPIV can handle particle image data of very high ppp levels (beyond 0.12) at which any single-particle tracking scheme failed to converge. Inspired by the successful practice in optical flow estimation, we implemented a coarse-to-fine estimation scheme combined with the median filtering of the estimated velocity field. The added trick is able to handle large displacement and can significantly boost the performance of our proposed approach. LAPIV can deal with both time-resolved and two-pulse data. Although labeled as a PIV approach, LAPIV can also produce accurate particle positions. This feature is particularly relevant for very high ppp data. The results will be shown during the workshop.

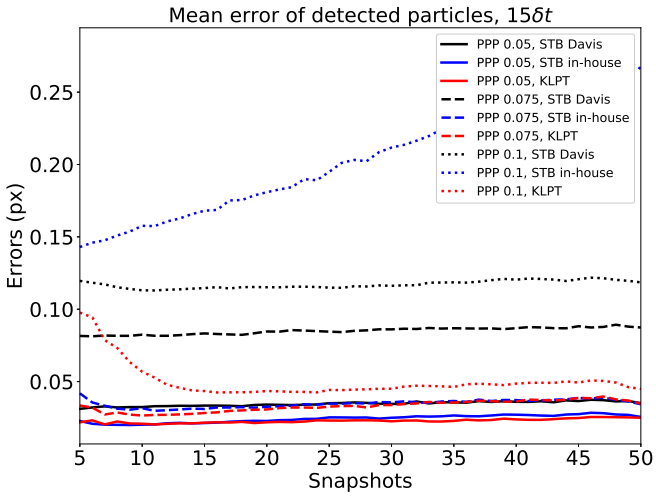

Fig. 1 Synthetic test result on mean error of detected particles.

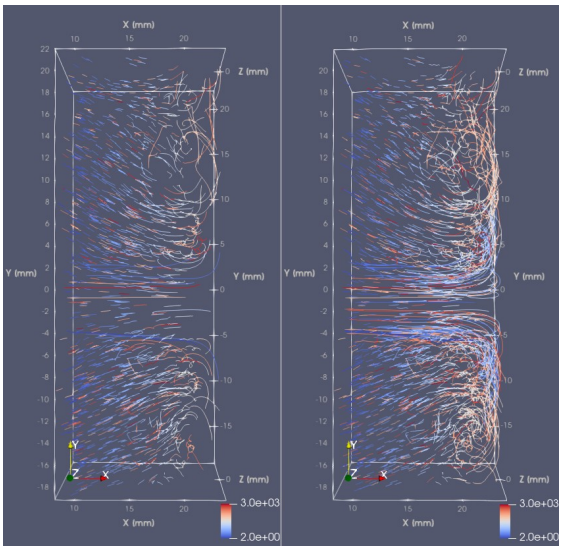

Fig. 2. The particle tracks of the first 3000 reconstructed particles visualized at the 50th snapshot: left, STB in Davis, right, KLPT.

References

Schanz, D., Gesemann, S., & Schröder, A. (2016). Shake-The-Box: Lagrangian particle tracking at high particle image densities. *Experiments in fluids*, *57*(5), 70.

Novara, M., Schanz, D., Reuther, N., Kähler, C. J., & Schröder, A. (2016). Lagrangian 3D particle tracking in high-speed flows: Shake-The-Box for multi-pulse systems. *Experiments in Fluids*, *57*(8), 128.

Novara, M., Schanz, D., Geisler, R., Gesemann, S., Voss, C., & Schröder, A. (2019). Multi-exposed recordings for 3d lagrangian particle tracking with multi-pulse shake-the-box. *Experiments in Fluids*, *60*(3), 1-19.

Tan, Shiyong, Ashwanth Salibindla, Ashik Ullah Mohammad Masuk, and Rui Ni. (2020). Introducing OpenLPT: New Method of Removing Ghost Particles and High-Concentration Particle Shadow Tracking. *Experiments in Fluids* 61(2): 47.

Wieneke, B. (2012). Iterative reconstruction of volumetric particle distribution. *Measurement Science and Technology*, *24*(2), 024008.

Schröder, A., Willert, C., Schanz, D., Geisler, R., Jahn, T., Gallas, Q., & Leclaire, B. (2020). The flow around a surface mounted cube: A characterization by time-resolved PIV, 3D Shake-The-Box and LBM simulation. *Experiments in Fluids*, *61*(9), 189.

Parnaudeau, P., Carlier, J., Heitz, D., & Lamballais, E. (2008). Experimental and numerical studies of the flow over a circular cylinder at Reynolds number 3900. *Physics of Fluids*, *20*(8), 085101.

Gesemann, S., Huhn, F., Schanz, D., & Schröder, A. (2016, July). From noisy particle tracks to velocity, acceleration and pressure fields using B-splines and penalties. *In 18th international symposium on applications of laser and imaging techniques to fluid mechanics*, Lisbon, Portugal

Schneiders, J. F. G., & Scarano, F. (2016). Dense velocity reconstruction from tomographic PTV with material derivatives *Experiments in Fluids*, *57*(9), 1–22.

Jeon, Y. J., Schneiders, J. F. G., Müller, M., Michaelis, D., & Wieneke, B. (2018). 4D flow field reconstruction from particle tracks by VIC+ with additional constraints and multigrid approximation. *ISFV 18*.

Yang, Y., Heitz, D., & Mémin, E. (2019).Lagrangian particle image velocimetry. In 13th International Symposium on Particle Image Velocimetry, *ISPIV 2019*.

3rd Workshop and Challenge on Data Assimilation & CFD Processing for PIV and LPT
November 19-20, 2020, virtual online meeting

Lagrangian Coherent Track Initialisation

Ali RAHIMI KHOJASTEH[1], Dominique HEITZ[1], Yin YANG[1] and Sylvain LAIZET[2]
[1] INRAE, UR OPAALE, Rennes Cedex F-35044, France

ali.khojasteh@inrae.fr
[2] Department of Aeronautics, Imperial College London, London, United Kingdom

Abstract

A coherency-based algorithm to build new tracks from local Lagrangian information of particles is introduced. In Lagrangian Coherent Track Initialisation (LCTI), we mainly concentrated on how to initialise first four-time steps, new entries and lost tracks, by a physics-based iterative forward-backwards four frame technique as a complementary function of Kernelized Lagrangian Particle Tracking (KLPT) [1] and Shake The Box (STB) [2]. Methods like as KLPT and STB require initial tracks to start predicting and optimising trajectories. More accurate initialisation technique could prevent the algorithm from failing or improve the convergence speed. Moreover, particles are continuously entering into the domain, which means, no matter how effective the algorithm can track a specific number of particles, new trajectories must be fed into the tracked pool. Otherwise, all tracked particles would leave the domain and at some point, there would be no new tracks. In the case of having complex flow motion, some particles lose their trajectories at the end of each time step. It is vital to return those lost particles into the tracked pool since an increasing number of lost tracks will increase the chance of being ignored by the algorithm as ghost or noise. The idea is that new entry and lost particles follow the same behaviour of their surrounding neighbours which means a new track is built if the trajectory is coherent with other neighbour tracks.

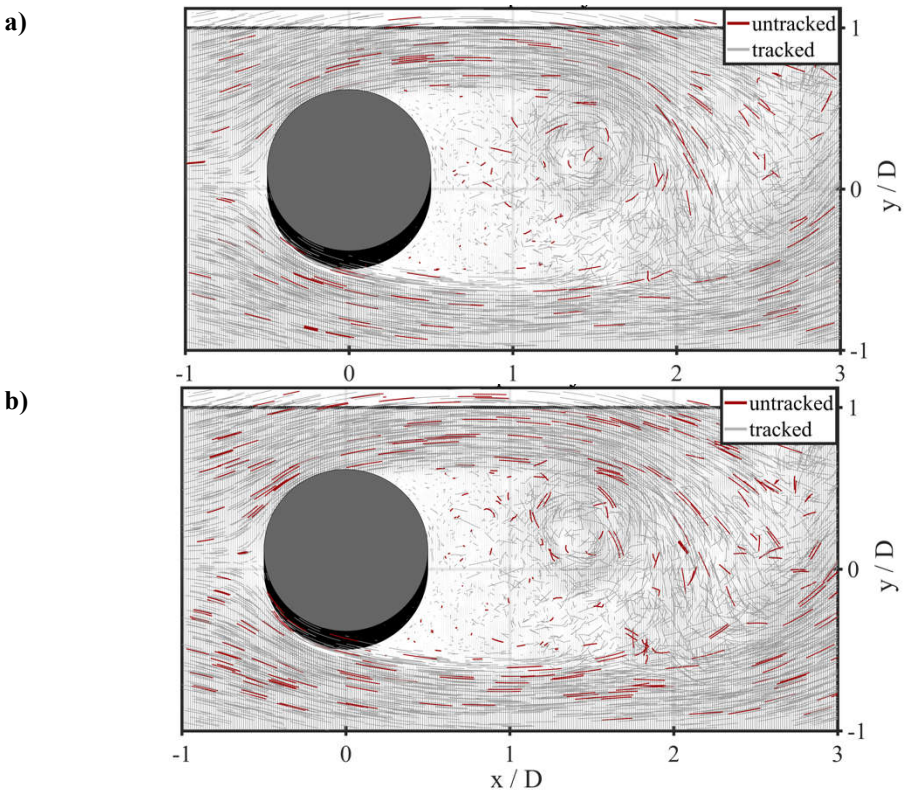

Fig. 1 Top view of 3D flow behind a cylinder, True track detection comparison between **a)** using Lagrangian Coherent Track Initialisation (LCTI) and **b)** Enhanced Track Initialisation (ETI), red lines are trajectories either untracked or mistracked, and grey lines are true tracks. Eulerian vector field is in the background.

Four frame track initialisations methods have been recently developed such as Enhanced Track Initialisation (4BE-ETI [3]) by looking for all track possibilities or four-frame best estimate (4BE) [4] by looking for nearest neighbours in frames until a unique track is found. The current coherency-based initialisation technique is following the same four frame approach but tries to find a coherent solution instead unique solution. Coherent refers to a group of particles which are spatially and temporally having same Lagrangian behaviour. This requires a function to determine information of coherent and non-coherent locally. There are many available concepts to identify Lagrangian Coherent Structures (LCS) [5] from estimating separatrix lines or surfaces which divide structures into different coherent regions. In Lagrangian frames, separatrices can be achieved from a scalar value called Finite-Time Lyapunov Exponent (FTLE) [5] by measuring the amount of stretching between the target particle and its neighbour particles over the time [6]. If a possible track is coherent with nearest tracks, then it will be indexed into track pool. This process continues iteratively until no track is found to be coherent with track pool.

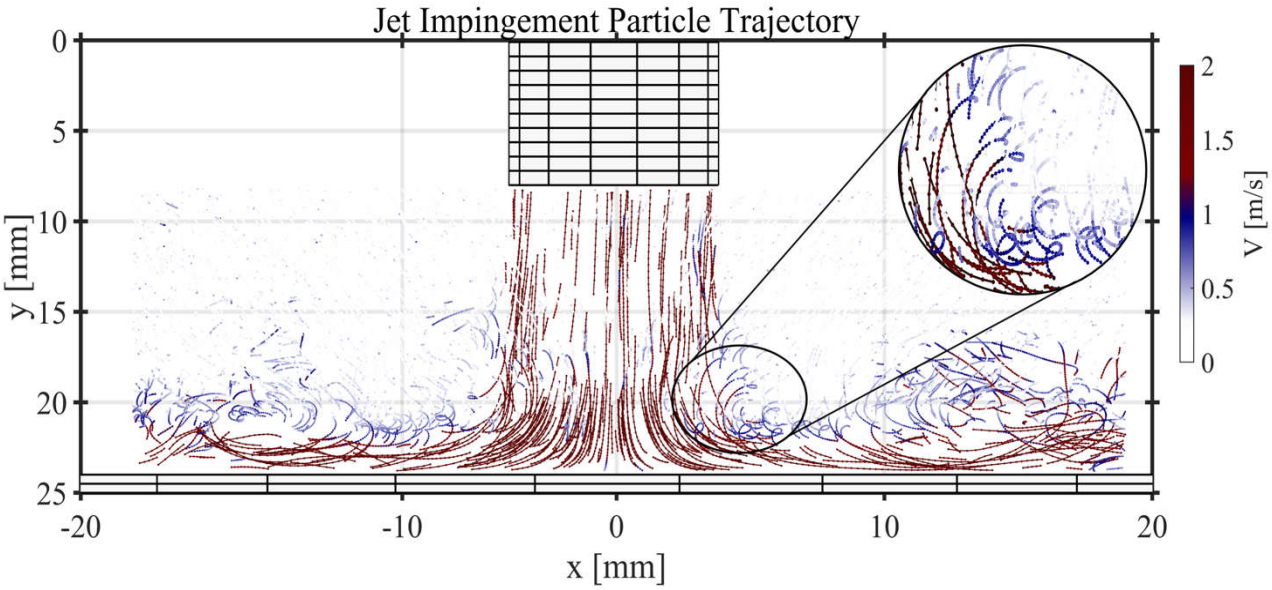

Fig. 2 Side view of particle trajectories colored by velocity magnitude in Jet Impingement at 0.03 ppp, low-velocity tracks away from the jet core are filtered for clear qualitative view thanks to the colorbar.

LCTI was tested using synthetic data over a cylinder obtained from 3D direct numerical simulation (DNS) at Reynolds number of 3900 and experimental jet impingement flow at Reynolds number of 2500. Both ETI and LCTI were computed in long tracks for the sake of qualitative visualisation although they are four frames. Figure 1 shows improvements compared to ETI at 0.05 ppp in a slice of 4D*2D*2D. High level of shear and velocity gradients exist in both sides of the vortex formation region in which LCTI has over 10 per cent more true tracks. Meanwhile, there is higher accuracy in track detection where the vortices are formed. Figure 2 also shows particle trajectories when a high accelerated jet impinges into a solid. The proposed method is able to follow complex motions such as vortex rings around the jet that their signatures can be seen from particle motions.

References

[1] Y Yang; D Heitz, "Kernelised Lagrangian Particle Tracking (KLPT) and Lagrangian PIV," *3rd Work. Chall. Data Assim. CFD Process. PIV LPT*, Nov 2020.

[2] D. Schanz, S. Gesemann, and A. Schröder, "Shake-The-Box: Lagrangian particle tracking at high particle image densities," *Exp. Fluids*, vol. 57, no. 5, May 2016.

[3] A. Clark, N. MacHicoane, and A. Aliseda, "A quantitative study of track initialization of the four-frame best estimate algorithm for three-dimensional Lagrangian particle tracking," *Meas. Sci. Technol.*, vol. 30, no. 4, 2019.

[4] N. T. Ouellette, H. Xu, and E. Bodenschatz, "A quantitative study of three-dimensional Lagrangian particle tracking algorithms," *Exp. Fluids*, vol. 40, no. 2, pp. 301–313, Feb. 2006.

[5] G. Haller, "Lagrangian coherent structures in," *Annu. Rev. Fluid Mech.*, pp. 1–19, Aug 2015.

[6] J. Brandon and E. Ott, "Chaos in Dynamical Systems," *Math. Gaz.*, vol. 79, no. 484, p. 233, 1995.

3rd Workshop and Challenge on Data Assimilation & CFD Processing for PIV and LPT
November 19-20, 2020, virtual online meeting

AI-based data assimilation: sound level spectra from time-resolved 3D LPT

Dong Kim[1] and Kyung Chun Kim[1]
[1]School of Mechanical Engineering, Pusan National University, Busan 46241, Republic of Korea
kckim@pusan.ac.kr

Abstract

This paper proposes a data assimilation method based on artificial intelligence (AI) to increase the spatial and temporal resolution of time-resolved three-dimensional Particle Tracking Velocimetry (4D PTV) data. Learning 3D or 4D flow patterns through AI can result in excellent generalization ability of the resulting model and a decrease in error and noise because it learns statistical data based on the neural network algorithm, which can be stored in a database. The 4D PTV was adopted to measure the instantaneous velocity field of a side-view mirror model in a wind tunnel (Kim et al., 2020). Helium-filled soap bubbles were used as tracers and the Shake-The-Box algorithm was used for particle tracking from images obtained by four high-speed cameras. The ensemble-averaged velocity fields and the features of vortex structures were analyzed. The 4D pressure fields were calculated by solving a Poisson equation using on the 4D PTV data. The temporal and spatial resolutions of the velocity and pressure field were increased using an Adaptive Neuro-Fuzzy Inference System (ANFIS) with the experimental data as a ground truth to predict wake flow behind the model. The ANFIS parameters were optimized as 300 epochs and a percentage of training data of 70%. The high-resolution ANFIS model was used to obtain the power spectra of the sound-pressure level spectra of the flow pressure fluctuations to examine the flow and noise characteristics of the side-view mirror model. To determine the three-dimensional flow structure and noise characteristics of the side-view mirror model, the instantaneous velocity and pressure field were deduced from the high-resolution ANFIS model. Vortex shedding phenomena and flow-induced noise are discussed based on the power spectrum and sound pressure level spectra.

Fig. 1 presents the instantaneous streamwise vortex structures in the wake of the side mirror model. Compared to the ensemble-averaged results (Fig. 1 (a) and (b)), the effects of data assimilation were certainly apparent. The AI-based data assimilation results (Fig. 1 (c)-(f)) showed much smaller vortex structures as a result of the four-fold increase in the spatial resolution. Moreover, the four-times higher temporal resolution of the ANFIS model revealed much more small-scale streamwise vortical structures than those from only an enhancement of the spatial resolution. These data assimilation results provide a better understanding of the small turbulence structures and allow for more in-depth analysis by recovering the missed data due to the resolution limit of the experiment. The ANFIS-based machine-learning algorithm worked well for finding the hidden three-dimensional vortical structures.

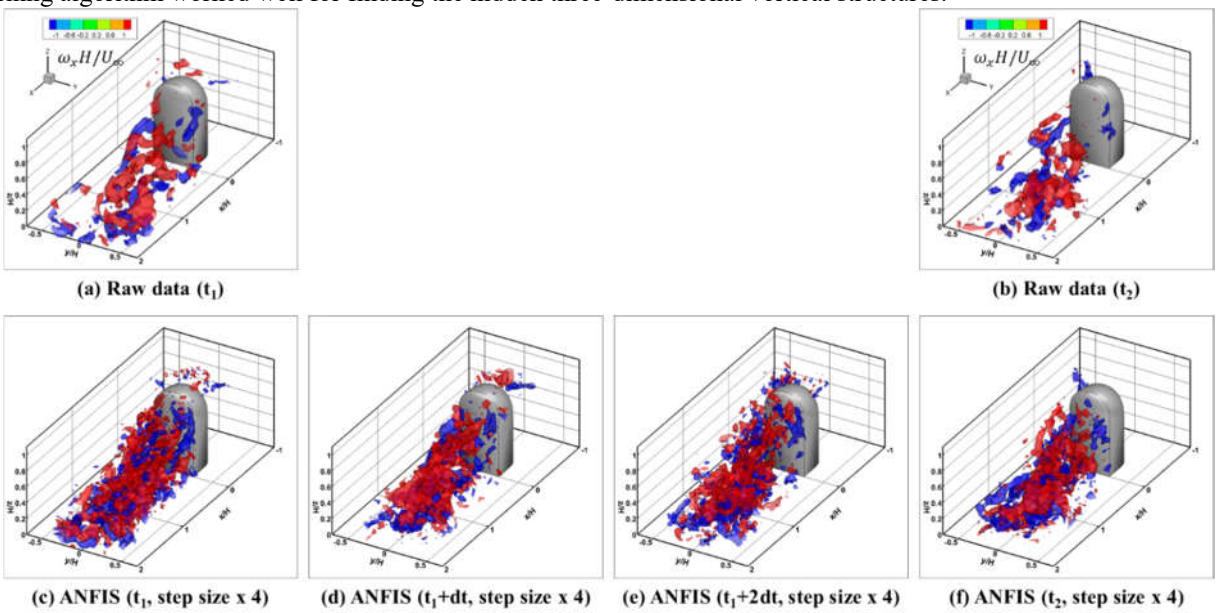

Fig. 1 Comparison of the instantaneous 3D streamwise vortex structures between the raw and assimilated data

From the ANFIS model with improved temporal and spatial resolution, it was possible to extract the instantaneous velocity and pressure fluctuations at a specific location in the flow field. After obtaining the power and noise level spectrum from the time series data, it was possible to obtain the shedding frequency of the vortex from the side mirror model and identify the noise source from the fluctuation of the flow pressure. Fig. 2 shows three locations where the velocity and pressure are extracted from the horizontal plane at z/H = 0.5. Position 1 (P1) is in the recirculation zone (x/H = 0.2, y/H = -0.2), where backflow occurs behind the model. Position 2 (P2) is located at the wake shear layer region (x/H = 0.5, y/H = -0.3) with a high streamwise velocity. Position 3 (P3) is in the area where the trailing vortex appeared near the central region (x/H = 1.0, y/H = -0.1) of the wake after passing the recirculation zone downstream of the model.

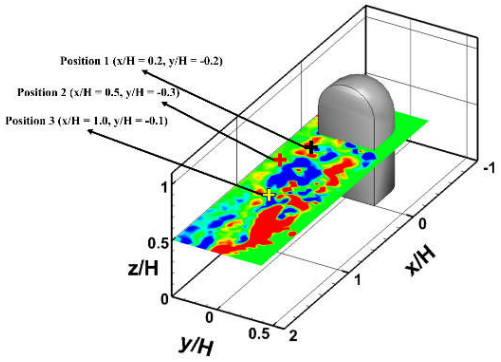

Fig. 2 Measurement positions at z/H = 0.5

Fig. 3 (left) compares the instantaneous pressure extracted from the raw data and the ANFIS model with a four-fold higher temporal resolution. For a better comparison, only 1.5 seconds was selected. The overall change coincided with each other, but the pressure signal from the ANFIS model appeared smoother.

Fig. 3 (right) compares the SPL spectra for different positions behind the side mirror model. The magnitude of the noise level was highest at P1, followed by P2 and P3. In Fig. 4, the SPL spectra obtained using the raw pressure data and the instantaneous pressure extracted from the ANFIS model were compared. The SPL level spectrum obtained using the raw data revealed a noisy spectrum, whereas that from the ANFIS model depicted a smooth spectrum. The peaks of SPL are dominant at 10 - 200 Hz in the low-frequency band. This region showed strong air resonance, and most of the noise felt by humans was in this band. At P1, the peak frequencies were found at 10, 20, 40, 80, and 120 Hz, which are the harmonics based on 10 Hz. At P2, the peak sound frequencies were observed at 50, 100, and 200 Hz, which are the harmonics of vortex shedding frequency, 50 Hz. At P3, peaks appeared at 100 and 200 Hz, the same as P2, which can be expected from the similar pressure fluctuations shown in Fig. 3.

The AI-based data assimilation method demonstrated a good candidate for a 4D PTV post-processing method that provides a better understanding of the small turbulence structures and allows for more in-depth analysis by recovering the missed data due to the resolution limit of the experiment. On the other hand, the accuracy was highly dependent on the raw data, which was used as the ground truth. To provide a full turbulence spectrum, higher-resolution 4D PTV data will be necessary for ANFIS training. Further research will be needed to find a super-resolution AI model to resolve the Kolmogorov scale of turbulent flows with high computing power.

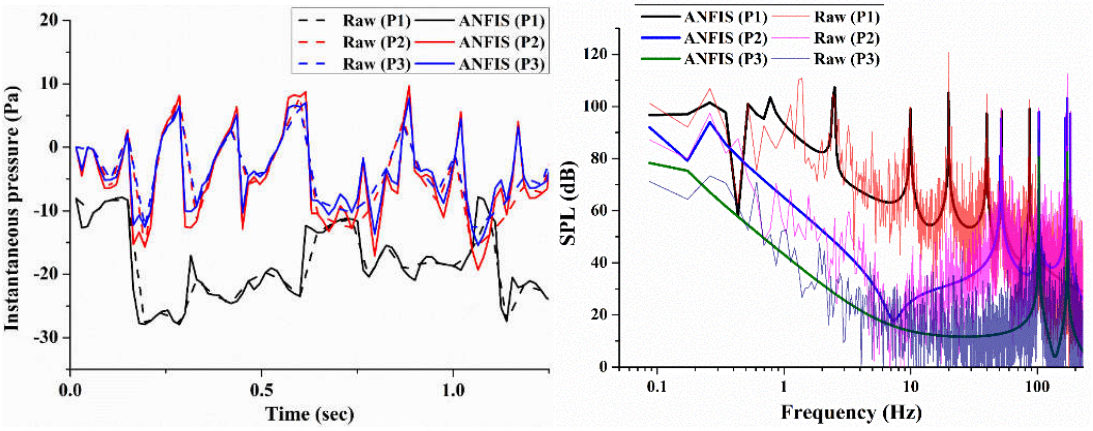

Fig. 3 Comparison of the instantaneous flow pressure fluctuations (left) and sound pressure level spectrum (right) between raw and assimilated data taken at P1, P2, and P3 in the horizontal plane at z/H = 0.5

References

Kim D, Kim M, Saredi E, Scarano F, Kim K. C (2020) Robotic PTV study of the flow around automotive side-view mirror models. Experimental Thermal and Fluid Science. 119(1):110202. https://doi.org/10.1016/j.expthermflusci.2020.110202

3rd Workshop and Challenge on Data Assimilation & CFD Processing for PIV and LPT
November 19-20, 2020, virtual online meeting

Sequential Data Assimilation for Unsteady Flow Pressure Determination Using Continuous Adjoint Formulation

Chuangxin He[1,2,*] and Yingzheng Liu[1,2]
1 Key Lab of Education Ministry for Power Machinery and Engineering,
School of Mechanical Engineering, Shanghai Jiao Tong University, Shanghai, China
2 Gas Turbine Research Institute, Shanghai Jiao Tong University, Shanghai 200240, China

* chuangxin.he@sjtu.edu.cn

Abstract

A sequential data assimilation (DA) method is proposed based on the contineous adjoint formulation. A forcing F, which need to be optimized using the adjoint system, is added to the primary Navier-Stokes (N-S) equations to drive the assimilated flow toward the observations at each time step. Compared to the four-dimensional variational method (4DVar) which requires the forward integration of the primary system and the backward integration of the adjoint system, the present approach integrates the primary-adjoint system all the way forward, discarding the requirement of data storage at every time step and being less computational consuming and space saving. This sequentionla DA method is applied in the pressure determination from turbulent velocity fields measured by particle image velocimetry (PIV). The pressure determination method of integration from eight paths (Dabiri et al., 2014) is also involved for comparison. While the integration method shows significant overprediction of the pressure in the wake region in flow over a circular cylinder due to the small size of the flow field of view, the present DA scheme recovers the pressure field quite well. Using the synthetic PIV data of a turbulent jet as the observation, the present DA method is able to determine the instantaneous pressure field precisely using the three-dimensional velocity fields regardless of the observational noise. For the two-dimensional three-component (3C) or two-component (2C) velocity fields, which are not sufficient for the pressure determination in integration method due to the lack of the off-plane derivatives, the present DA method is able to reproduce the pressure fields whose statistics agree reasonably well with that of the referential results. Whereas, the 3C and 2C velocity fields yield quite similar results, indicating the possibility of the pressure determination from planar-PIV measurement in turbulent flows. The tomography PIV (tomo-PIV) measurement is also tested as the observation, while a clear pressure pattern is obtained by the present DA method.

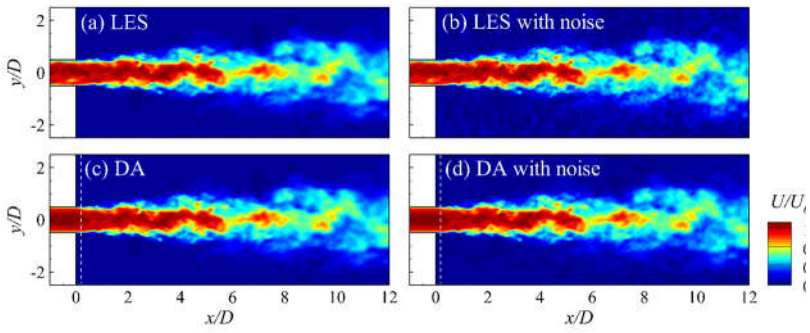

Fig.1 Velocity fields obtained by (a-b) LES and (c-d) DA. The observation region locates in the downstream of the dashed line.

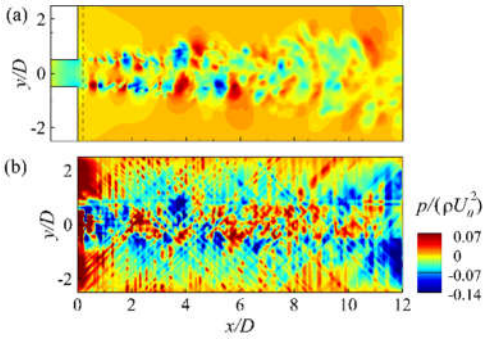

Fig. 2 Instantaneous pressure fields obtained by (a) DA and (b) integration

References

1. S. Pröbsting, F. Scarano, M. Bernardini, and S. Pirozzoli, "On the estimation of wall pressure coherence using time-resolved tomographic PIV," Experiments in fluids 54, 1567 (2013).
2. J. J. Charonko, C. V. King, B. L. Smith, and P. P. Vlachos, "Assessment of pressure field calculations from particle image velocimetry measurements," Measurement Science and technology 21, 105401 (2010).
3. C. He, Y. Liu, and L. Gan, "A data assimilation model for turbulent flows using continuous adjoint formulation," Physics of Fluids 30, 105108 (2018).
4. M. Lemke, and J. Sesterhenn, "Adjoint-based pressure determination from PIV data in compressible flows—validation and assessment based on synthetic data," European Journal of Mechanics-B/Fluids 58, 29 (2016).

3rd Workshop and Challenge on Data Assimilation & CFD Processing for PIV and LPT
November 19-20, 2020, virtual online meeting

Nudging the Reynolds-Averaged Navier-Stokes equations with synthetic PTV-data of the square cylinder flow at Re=22 000.

Markus Zauner[1], Vincent Mons, Olivier Marquet and Benjamin Leclaire

DAAA - Aerodynamics Aeroelasticity Acoustics, ONERA, Meudon, France
[1]mzauner@onera.fr

Abstract

Data-assimilation aims at combining experimental and numerical approaches to obtain more detailed solutions of complex flow fields, maintaining high fidelity with reasonable computational efforts. While adjoint-based data-assimilation delivered promising results for laminar flows (Gronskis et al. 2013), the numerical cost of the optimization process becomes prohibitive for unsteady turbulent flows. In that case, we may consider a much simpler data-driven approach called "nudging" or "state estimator/observer", originally introduced in the fields of meteorology or control theory, where partial field measurements are introduced as a feedback term to control the evolution of the governing equations. Using experimental wall-pressure measurements or Particle Tracking Velocimetry (PTV) data, Nisugi et al. (2004) and Yamagata et al. (2008) successfully used this method to reconstruct the low-Reynolds laminar flow around a squared cylinder. More recently, Di Leoni et al. (2020) performed a nudging of the three-dimensional unsteady Navier-Stokes equations to reconstruct large and small-scale structures in the canonical homogeneous and isotropic turbulent flows. To limit the computational cost, the Reynolds-Averaged Navier-Stokes equations closed with a turbulence model are often used to model aerodynamic flows. We propose here to reconstruct dense velocity and pressure fields around a square cylinder flow at Reynolds number Re=22,000 by nudging the Unsteady Reynolds-Averaged Navier-Stokes (URANS) equations with sparse unsteady velocity measurements.

Following the terminology introduced by Di Leoni et al. (2020), a Lagrangian nudging is considered in the present contribution since the sparse data are obtained from a PTV measurement of velocity fields obtained with direct numerical simulation (DNS). A local feedback forcing is then introduced in the momentum URANS equations, that can be rewritten as

$$\frac{\partial \boldsymbol{u}}{\partial t} + (\boldsymbol{u}\cdot\boldsymbol{\nabla})\boldsymbol{u} = -\frac{1}{\rho}\boldsymbol{\nabla} p + \boldsymbol{\nabla}\cdot[(\nu+\nu_t)\boldsymbol{\nabla_S}\boldsymbol{u}] + \alpha h^T(h(\boldsymbol{u})-m),$$

where ν and ν_t denote the molecular and turbulent viscosity, respectively. The Spalart-Allmaras model is used here to determine the turbulent viscosity. The parameter α denotes the magnitude of the nudging term, the latter being non-zero only at positions of the PTV measurements. Here, it is proportional to the difference between the true/experimental velocity data m and the measured velocity field $h(\boldsymbol{u})$, where the operator h projects the numerical velocity field onto the measurement space and might also account for its spatial resolution. By marching in time these equations with measurement data available at each time step, we investigate how the solution of the URANS equations converges towards the DNS solution. The latter is also used to quantify the performance of this data-assimilation approach independently of the number of sampling points used for the nudging.

Preliminary results of the flow reconstruction are shown in Figure 1. Figure 1(a) shows the lift coefficient C_L as a function of time for the true solution (DNS) and standard URANS solution denoted by black and blue curves, respectively. While the initial solution for URANS is chosen to qualitatively match the DNS flow field at $t=0$, we observe the phase between both histories shifting with increasing simulation time. This is also visible in figure 1(b) comparing snapshots of vorticity fields obtained at three instants (in columns) with the different flow models (in rows). When comparing contours of top and middle rows corresponding to the standard URANS and DNS method, respectively, we can observe the phase difference developing in the wake due to discrepancies in the shedding frequency of the vortex street. Firstly, we select a fixed set of grid points (indicated by the black dots in the contour plot of the middle row in figure 1b), where we sample velocity data from the DNS at each URANS time step. This data is now used to nudge the URANS equations at these specified positions, while the nudging term is zero elsewhere. Using 680 sampling points out of 46,228 grid points is sufficient to synchronize the nudged simulation with the DNS. Differences with respect to the true velocity field are not only reduced at sampling positions, but also at locations where no sampling data is available. The bottom row of figure 1(b) showing nudged vorticity fields agrees qualitatively well

with the true solution corresponding to DNS data (middle row). The lift coefficient of nudged and standard URANS methods is shown in figure 1(c) corresponding to red and blue curves, respectively. The red curve in figure 1(c) agrees very well with the black curve in figure 1(a).

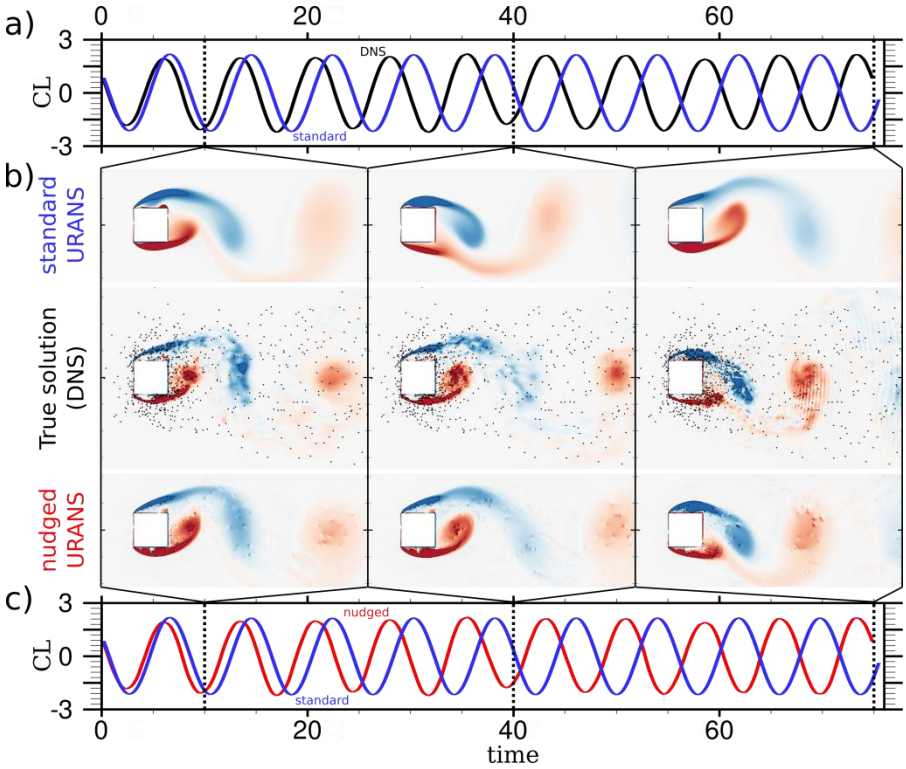

Figure 1: (a) The lift coefficient CL as a function of time for DNS (black) and standard URANS methods (blue). (b) Representative vorticity snapshots for standard URANS (top row), DNS (middle row), and nudged URANS (bottom row). (c) The lift coefficient CL as a function of time for nudged (red) and standard (blue) URANS methods.

Secondly, we randomly change the location of sampling points for each time step. As the sampling data between consecutive time steps is uncorrelated, we consider this test case as a "worst-case" scenario mimicking PTV data. Even though the integral error is higher compared to the Eulerian test case described above (not shown here), we are still able to synchronize the nudged URANS simulation with DNS data and significantly improve standard URANS results.
Future work will be dedicated to use simulated Lagrangian PTV data instead of random uncorrelated sampling point and to post-process the DNS data so as to select the large-scale flow features that are modelled by the RANS equations.

Acknowledgments

This project is funded by the European Union's Horizon 2020 research project entitled "HOMER - Holistic Optical Metrology for Aero-Elastic Research" under grant agreement No 769237. The authors would also like to acknowledge Dr. Julien Dandois for providing us DNS data.

References

Gronskis, A., Heitz, D., & Mémin, E. (2013). Inflow and initial conditions for direct numerical simulation based on adjoint data assimilation. *Journal of Computational Physics*, *242*, 480-497.
Di Leoni, Clark Patricio, Mazzino, Andrea & Biferale, Luca (2020) Synchronization to Big Data: Nudging the Navier-Stokes Equations for Data Assimilation of Turbulent Flows. Physical Review X10(1), 011023, arXiv: 1905.05860.
Nisugi, Keisuke, Hayase, Toshiyuki & Shirai, Atsushi (2004). Fundamental study of hybridwind tunnel integrating numerical simulation and experiment in analysis of flow field. *JSME International Journal, Series B: Fluids and Thermal Engineering*, 47(3), 593–604.
Yamagata, Takayuki, Hayase, Toshiyuki & Higuchi, Hiroshi (2008). Effect of Feedback Data Rate in PIV Measurement-Integrated Simulation. *Journal of Fluid Science and Technology* 3(4), 477–487.

3rd Workshop and Challenge on Data Assimilation & CFD Processing for PIV and LPT
November 19-20, 2020, virtual online meeting

Eulerian time-marching in Vortex-In-Cell (VIC) method by optimizing 4D boundary conditions

Young Jin Jeon
LaVision GmbH, Göttingen, Germany
yjeon@lavision.de

Abstract

A data-assimilation approach is proposed to enhance the dynamic range by increasing a ratio of the number of PTV vectors to the number of unknowns. This approach is fundamentally based on the Vortex-In-Cell (VIC) method (Christiansen 1973, Ould-Salihi et al. 2000, Morgenthal and Walther 2007, and others). The VIC method derives a flow field on a Cartesian grid from a vorticity field through the Poisson equation with prescribed boundaries of velocity and acceleration. In addition to that, VIC is able to simulate a time-marching flow field using Lagrangian vortex particles. Using these features, Schneriders et al. (2014) successfully recover unmeasured time-steps between time-undersampled PIV snapshots. Instead of the Lagrangian time-marching fashion of VIC, the present approach proposes the Eulerian time-marching utilizing the vorticity time derivative, e.g., $\boldsymbol{\omega}\,(t + \Delta t) = \boldsymbol{\omega}\,(t) + \Delta t \cdot \partial\boldsymbol{\omega}/\partial t\,(t)$. Here, unlike the vorticity field, the boundary conditions have no potential to produce meaningful information through the time-marching because of their extrapolated and depleted information due to the distance from PTV realizations. Therefore, the optimization variables consist of not only a single vorticity field but also multiple boundaries as the number of input PTV snapshots. Consequently, an enhanced dynamic range can be expected when a large number of PTV snapshots are simultaneously considered.

The cost functions regarding the entire snapshots are evaluated by VIC# (Jeon et al. 2018), which supplements additional constraints and coarse-grid approximation to VIC+ (Schneiders and Scarano 2016). The velocity boundary is regularized by minimizing a difference between its discrete-time derivative and the acceleration to ensure that the optimization converges. The boundary conditions at fractional instances are interpolated based on second-order time discretization, i.e., linear interpolation for the acceleration. Additional adjoints concerning the time-marching and the boundary regularization are derived. Two time-marching schemes, i.e., the Euler method and the Runge-Kutta method, are introduced. The present method is implemented in a graphic processing unit (GPU) for computational speed.

The numerical assessment is conducted by synthetic PTV data, whose ground truth is known. Fig. 1 visually compares reconstructions from the VIC# and the present method with the reference. It is shown that the present approach well recovers the minor vortical structures and thus the connections between isolated ones as well.

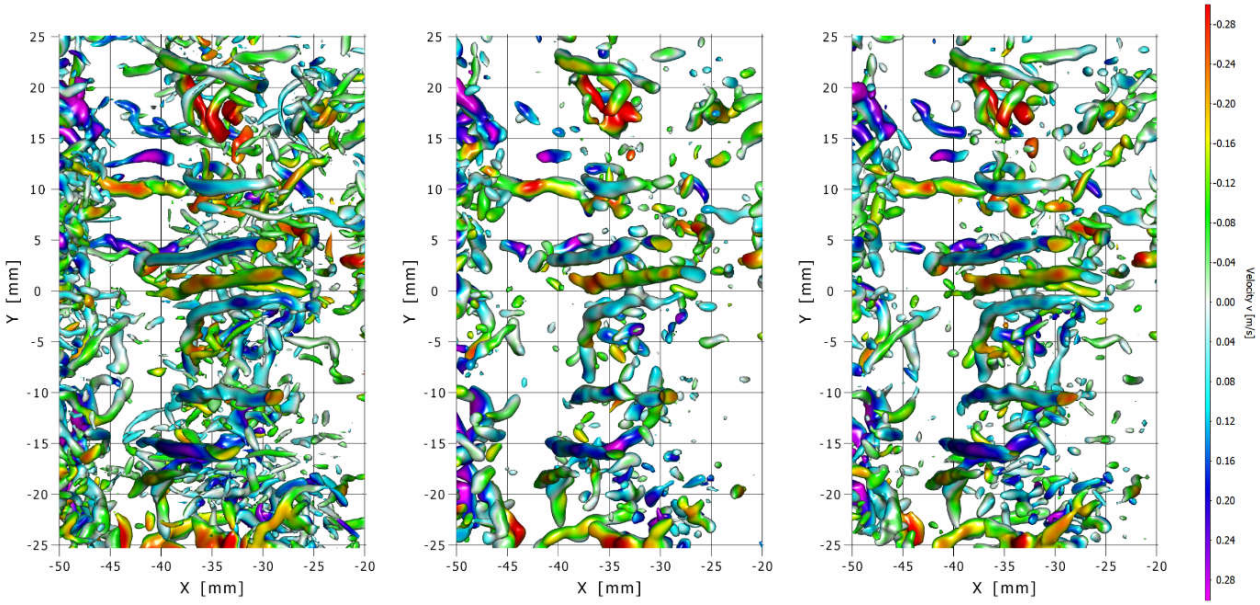

Fig. 1 Flow structures visualized by iso-surfaces of $\lambda_2 = -30{,}000\ s^{-2}$: LES reference (left), VIC# from a single PTV snapshot (middle), and the present method from 13 PTV snapshots using the Runge-Kutta method (right)

Fig. 2 shows the root-mean-square (RMS) error of velocity and the quality of swirling strength evaluated as the cross-correlation of negative λ_2 between the reference and the reconstructions. When no time-marching integration for fractional instances between consecutive PTV snapshots is conducted (M = 1), it is deemed that truncation errors are accumulated as the number of input PTV snapshots (L) increases. Here, M indicates a number of the time-marching integrations per one additional PTV snapshot. When the computation cost is same (M = 4), the Euler method and the Runge-Kutta method show similar error and quality curves.

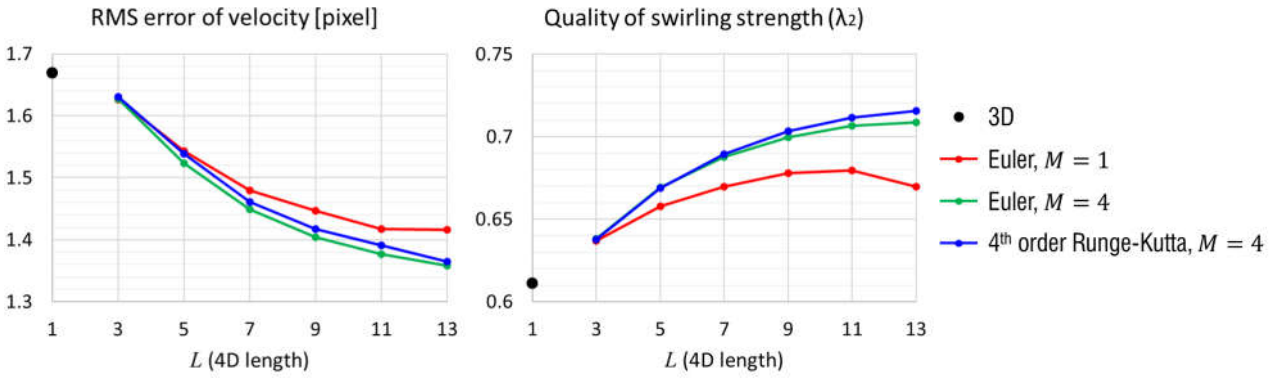

Fig. 2 RMS error of velocity (left) and quality of swirling strength (right)

References

Christiansen JP (1973) Numerical simulation of hydrodynamics by the method of point vortices. Journal of Computational Physics 13:363–379

Ould-Salihi ML, Cottet G, and Hamraoui ME (2000) Blending finite-difference and vortex methods for incompressible flow computations. SIAM Journal on Scientific Computing 22:1655–1674

Morgenthal G and Walther JH (2007) An immersed interface method for the Vortex-In-Cell algorithm. Computers & Structures 85:712–726

Schneiders JFG, Dwight RP, and Scarano F (2014) Time-supersampling of 3D-PIV measurements with vortex-in-cell simulation. Experiments in Fluids 55:1692

Jeon YJ, Schneiders JFG, Müller M, Michaelis D, and Wieneke B (2018) 4D flow field reconstruction from particle tracks with additional constraints and multigrid approximation. In 18th International Symposium on Flow Visualization – ISFV18, Zurich, Switzerland, June 26-29

Schneiders JFG and Scarano F (2016) Dense velocity reconstruction from tomographic PTV with material derivatives. Experiments in Fluids 57:139

3rd Workshop and Challenge on Data Assimilation & CFD Processing for PIV and LPT
November 19-20, 2020, virtual online meeting

Velocity field reconstruction with time segment assimilation

Fulvio Scarano, Gabriel Gonzalez Saiz and Andrea Sciacchitano
Aerospace Engineering Department, TU Delft, Delft, The Netherlands
f.scarano@tudelft.nl

Abstract

The time-segment assimilation (TSA) method aims at refining the spatial reconstruction of the sparse velocity field obtained from 3D time-resolved motion analysis of fluid flow tracers. The method leverages upon the spatio-temporal information from a finite number of successive time samples of particle velocity, commonly denoted as *tracks*, coming from PTV or STB analysis (Maas et al. 1993; Schanz et al. 2016). The working principle and hypotheses introduced by Schneiders and Scarano (2018) are further discussed here, identifying three regimes of operation: in the sparse mode (figure 1-left) the length of the trajectories is small compared to the average distance between tracers. In the regime of adjacent tracks (figure 1-middle), the time segment length is such that the length of the tracks equals the particles distance. This regime is particularly interesting in that it significantly decreases the sparsity of measured data in terms of time-space distance. When the length of the time segment is further increased (figure 1-right), the spatial distance between tracks decreases, but the time distance increases. This regime is expected to increase marginally the quality (viz. resolution) of the reconstruction, and the overall benefit may be lost, due to the larger computational effort.

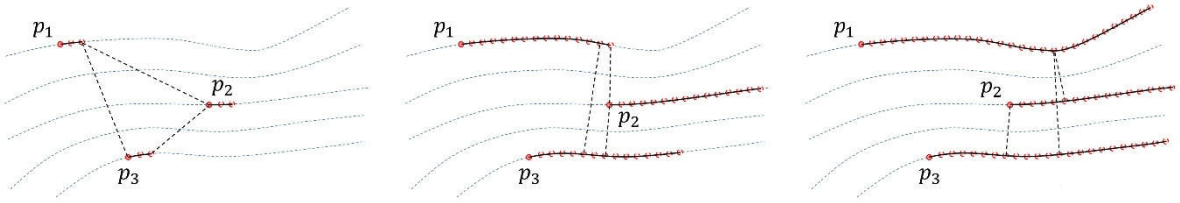

Fig. 1 Representation of the three working regimes for TSA. Left: three particles (p_1, p_2 and p_3) with short streak length (based on three recordings, N = 3). The streak length remains smaller than the distance (dashed lines) among neighbouring tracks. Middle: the streak length (N = 15) is comparable to the inter-particle distance, which reduces the distance between the considered tracks. Right: the streak length (N = 29) exceeds the inter-particle distance and the distance between tracks is reduced, yet marginally.

The working algorithm of TSA in terms of the data assimilation to the flow governing equations makes use of the vorticity transport equation in the inviscid incompressible regime, i.e.: $\partial\boldsymbol{\omega}/\partial t = (\boldsymbol{\omega}\cdot\nabla)\boldsymbol{u} - (\boldsymbol{u}\cdot\nabla)\boldsymbol{\omega}$.
The optimization process is based on the Vortex-in-Cell framework, similarly to the VIC+ methodology (Schneiders and Scarano, 2016). Therefore, a vortex-particle discretization is used for the numerical integration of the vorticity field, from which the velocity field at every instant of the assimilated time-segment is calculated by solving the Poisson equation $\nabla^2\boldsymbol{u} = -\nabla\times\boldsymbol{\omega}$.
The ability of TSA in delivering high-resolution velocity reconstructions is inquired by numerical and experimental assessments. A synthetic field of a 3D sine-wave lattice, popular among previous works, focuses on the amplitude modulation. The latter effect appears to be reduced when moving from the assimilation of a short time sequence, towards a longer time segment. Furthermore, it is observed that the result of the numerical process is independent of the time interval chosen for time-marching, provided that the CFL condition is respected.

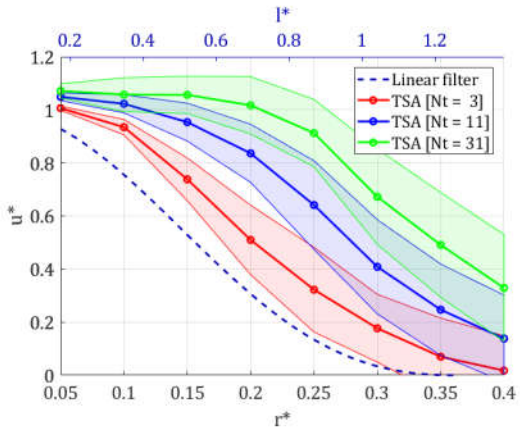

Fig. 2 Normalised velocity response u* to a sinusoidal distribution as a function of the inter-particles distance. The parameter r* is the normalised wavenumber, computed as the ratio between the average inter-particle distance and the flow wavelength. The parameter l* on the top axis represents the ratio between the linear size of the cubic element used as linear filter and the flow wavelength. The parameter N_t indicates the track length.

The experimental analysis is performed on data from a multichannel swirling jet (Ianiro et al. 2019). The analysis indicates that the vorticity field is enriched when the assimilation is conducted with a time segment corresponding to a streak length in excess of the particles average distance.

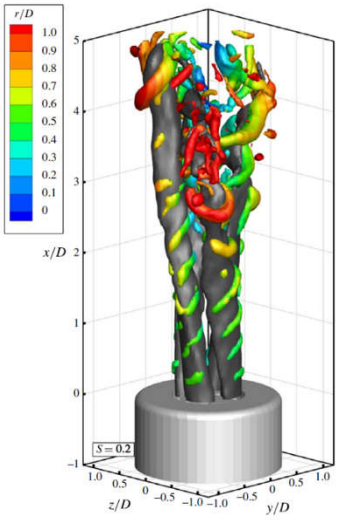

Fig. 3 Instantaneous velocity field (gray isosurface) and vortex structure (Q-criterion, radial distance as color coding) of a swirling jet. Baseline for data assimilation with TSA. (Repr. from Ianiro et al. 2018)

References

Ianiro A, Lynch KP, Violato D, Cardone G, Scarano F (2018). Three-dimensional organization and dynamics of vortices in multichannel swirling jets. *Journal of Fluid Mechanics. 843:180-210*.

Maas HG, Gruen A, Papantoniou D (1993). Particle tracking velocimetry in three-dimensional flows. *Experiments in fluids. 15(2):133-46*.

Schanz D, Gesemann S, Schröder A (2016). Shake-The-Box: Lagrangian particle tracking at high particle image densities. *Experiments in fluids. 57(5):70.*

Schneiders JFG, Scarano F(2016) Dense velocity reconstruction from tomographic PTV with material derivatives. *Experiments in Fluids. 57:139.*

Schneiders JFG, Scarano F, Elsinga E (2017). Resolving vorticity and dissipation in a turbulent boundary layer by tomographic PTV and VIC+. *Experiments in Fluids. 58:27.*

Schneiders JFG, Scarano F (2018). On the use of full particle trajectories and vorticity transport for dense velocity field reconstruction. *19th Int. Symp. Appl. Laser Imaging Tech. Fluid. Mech., Lisbon (PT)*

3rd Workshop and Challenge on Data Assimilation & CFD Processing for PIV and LPT
November 19-20, 2020, virtual online meeting

FlowFit3: Fast Data Assimilation for Recovering Instantaneous Details of Incompressible Flows based on scattered data

Sebastian Gesemann[1]
[1]Department of Experimental Methods, DLR, Göttingen, Germany
sebastian.gesemann@dlr.de

Abstract

This works presents an evolution of the FlowFit method for reconstructing incompressible flow fields (specifically velocity and pressure) based on scattered velocity and acceleration data. It can thus be used to process the data obtained from Lagrangian Particle Tracking (LPT) in order to recover structures of fluid motion. The goal of this development was to improve both accuracy and speed over its predecessor so this method can be used in experiments with large measurement domains and/or a high number of seeding particles. The method will be explained and assessed in comparison with its predecessor using synthetic data derived from fluid simulations.

FlowFit2 (Gesemann 2016) and FlowFit3 recover the flow fields by recasting the problem as a cost function minimization problem where the solution to this optimization problem represents the velocity and pressure fields that are consistent with the scattered data. But whereas in FlowFit2 we dealt with physical constraints such as mass conservation, momentum conservation and no-slip conditions only by penalizing constraint violations as part of the cost function (penalty method), FlowFit3 uses a mix of techniques to satisfy most of these constraints exactly (divergence & pressure Poisson equation) and greatly reduce other constraint violations (no-slip conditions). In addition, FlowFit3 uses a different set of base functions for a continuous representation of the flow field based on a staggered grid and mixed-order B-splines. This allows the divergence constraint to be satisfied exactly over the whole domain instead of just over a finite set of grid points. To satisfy all the constraints we employ all of the following techniques depending on the constraints:

(1) Substitution: Pressure is derived from velocity so that the Poisson equations for pressure are always satisfied automatically.
(2) Orthogonal Gradient Projection: The cost function's gradient is projected into a divergence-free linear subspace. Therefore, a gradient-based solver for the optimization problem will not be tempted to leave this subspace and the divergence will always stay zero everywhere.
(3) Augmented Lagrangian Method: This is a simplification of the method of Lagrange multipliers for constraint optimization where the Lagrange multipliers are not variables that are optimized but updated after each optimization pass (Hestenes, 1969). We use this to deal with conditions related to immersed boundaries (e.g. no-slip on a wall).

Techniques (1) and (2) both involve solving 3D Poisson problems on a cuboid domain with the same size and same homogeneous Dirichlet boundary condition. They only differ in the filter kernel for the Laplace operator. These types of problems can be very efficiently solved because the Eigen decomposition of the respective equation systems can be efficiently computed using 3D discrete sine transforms (DST), for example, using the popular FFTW library. See figure 1 for a graphical visualization of the cost function.

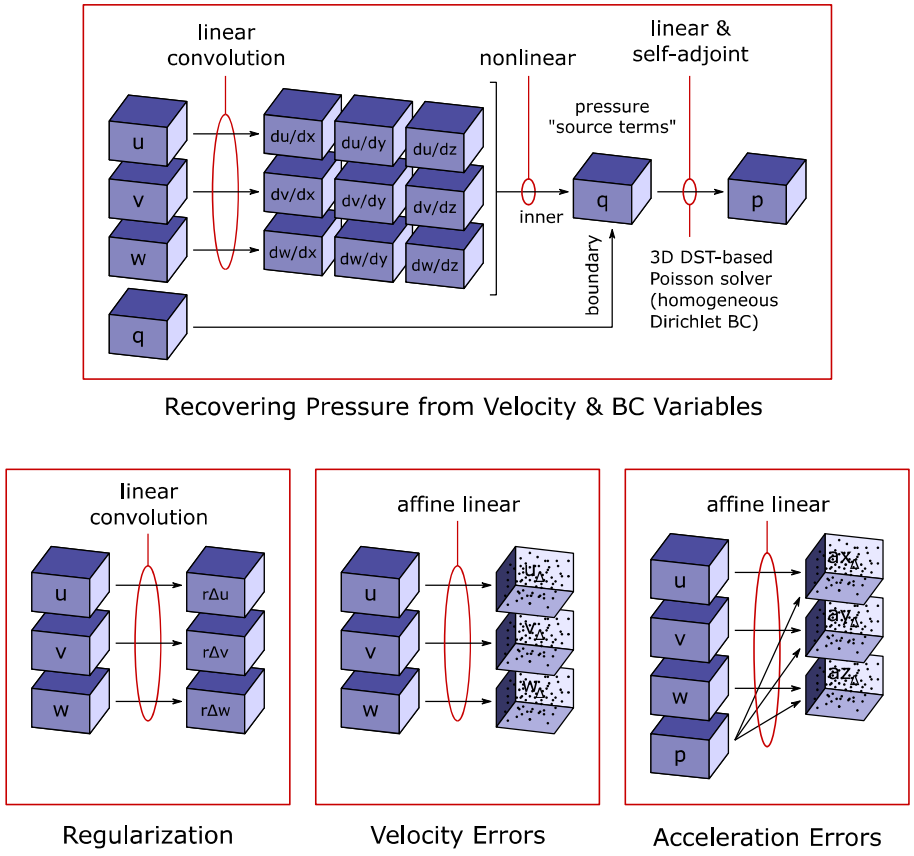

Fig. 1 Graphical representation of the cost function.

References

Hestenes M R (1969) Multiplier and gradient methods. Journal of Optimization Theory and Applications. 4: 303–320. doi:10.1007/BF00927673.

Gesemann S, Huhn F, Schanz D & Schröder A (2016) From noisy particle tracks to velocity, acceleration and pressure fields using B-splines and penalties. In 18th international symposium on applications of laser and imaging techniques to fluid mechanics, Lisbon, Portugal (pp. 4-7).

3rd Workshop and Challenge on Data Assimilation & CFD Processing for PIV and LPT
November 19-20, 2020, virtual online meeting

Development toward PSP-Driven CFD Simulation

Takao Suzuki
Mill Creek, WA, USA
takao.seattle@gmail.com

Abstract

Hybrid simulations combining PIV and DNS have successfully produced solutions of unsteady flows driven by time-resolved velocity measurements in the past studies [1,2]. This data-assimilation technique is able to suppress errors/noise associated with PIV data acquisition, to estimate unsteady pressure fields only from velocity measurement [3], and to generate a complete set of flow quantities compatible with the governing equations over time. Namely, we can replicate measured unsteady flow fields in a computational domain with the resolution and the compatibility equivalent to CFD solutions based on PIV data. This greatly enhances our post-processing capability of unsteady flows.

Likewise, we wish to assimilate unsteady surface pressure measurement into an unsteady CFD simulation (simpler ideas were explored in the past [4,5]). Recent pressure sensitive paint (PSP) techniques allow us to measure unsteady pressure variation on a painted surface at transonic Mach numbers, while the noise level is relatively high and the resolution is not as high as CFD. This study aims to develop a hybrid-simulation technique combining unsteady PSP and an unsteady compressible CFD solver. By forcing the pre-scribed surface pressure over a wall as the Dirichlet boundary condition, we solve the compressible Euler equation so that the PSP data rectify the CFD solution (see Fig. 1):

$$p^n_{\text{Hybrid}} = [1 - \varepsilon f(c)]\, p^n_{\text{Euler}} + \varepsilon f(c)\, p^n_{\text{PSP}}\,, \qquad (1)$$

where the surface pressure of the Euler solver p^n_{Euler} extrapolated from the flow field and that directly from the PSP measurement p^n_{PSP} are linearly combined via a weight function ε and a function $0 \le f(c) \le 1$ that specifies the measured surface region; subsequently, the flow field is marched by the unsteady CFD solver by imposing the hybrid surface pressure p^n_{Hybrid} on the wall. The hybrid simulation then finds a solution of the flow field that best fits the PSP measurement. As a result, we expect that this data-assimilation technique can suppress the measurement noise and enhance the spatial resolution of the measured pressure fields. More importantly, it expands surface measurement data into another dimension via CFD simulation.

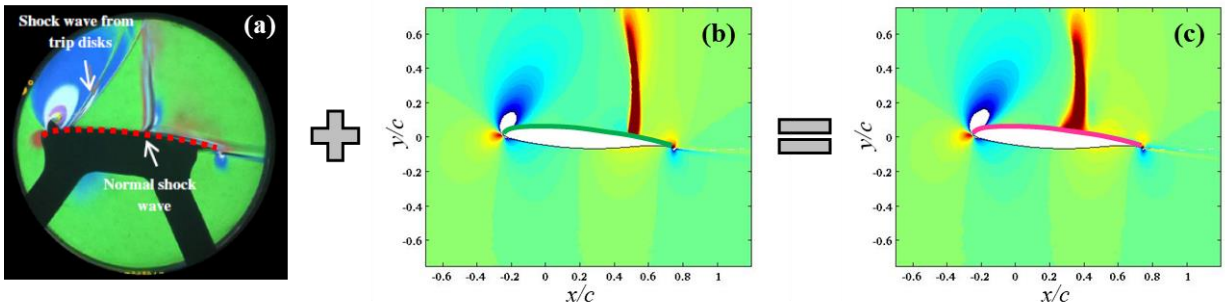

Fig. 1 *Illustration of the PSP-Driven hybrid simulation. (a) Schlieren photograph from [6]. PSP applied on the red dotted line. (b) Density gradient of 2D solution of the pure Euler-equation solver. (c) That of the hybrid simulation.*

As an example, we consider NASA CRM65 airfoil with a free-stream Mach number of $M_\infty = 0.74$ in two dimensions, and impose pre-scribed wall pressure on the suction side by hypothesizing that PSP data from [6] are available (we first force steady *Cp* at $\alpha = 5^o$). The Euler-equation solver adopts Roe's flux-difference-splitting scheme with a C-type mesh fitted with the tunnel height. The pure CFD

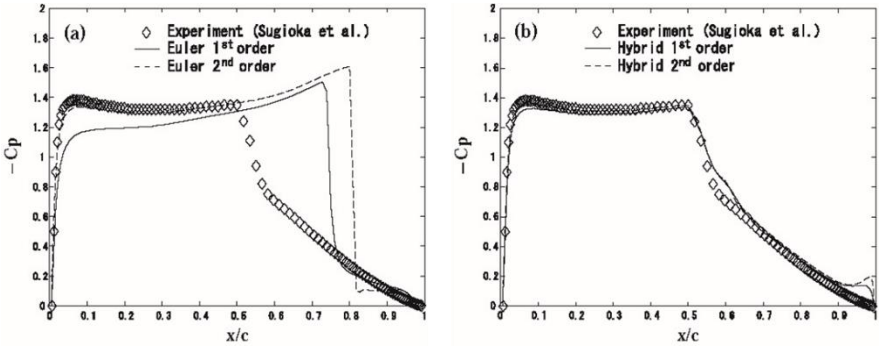

Fig. 2 *Comparison of the Cp profiles on the suction side of NASA CRM65 at $\alpha = 5^o$. (a) Euler-equation solvers versus the experiment from [6]. (b) Hybrid simulations versus the experiment.*

solver predicts the shock position more downstream (see Fig.1b computed by the 1st-order Euler-equation solver) than that measured in the experiment for an unknown reason (see Fig.1a). The 2nd-order Euler-equation solver, which has been verified with a NACA0012 benchmark problem [7], locates the shock even further downstream (see Fig. 2a, where the surface pressure in the CFD is evaluated at interior grid points). By assimilating the steady *Cp* profile given in [6] into the CFD solver, the hybrid simulation corrects the shock position not only on the airfoil surface but also away from the wall over the suction side: In fact, we can see the effect of the hybrid simulation on the surface *Cp* profiles in Fig. 2b and also the shock position in space, as compared with the Schlieren photograph (see Figs.1c and 1a). This example demonstrates that the hybrid simulation can properly drive the CFD solution by the steady PSP measurement.

Sugioka *et al.* [6] reported that $\alpha = 6^o$, the shock wave starts oscillating (see Fig. 16 in [6]), while the unsteady Euler-equation solver predicts a steady flow field, as shown in Fig. 3. To examine the capability of implementing unsteady PSP measurement in the hybrid simulation, we produce a synthetic *Cp* profile which sinusoidally switches between the time-averaged profile from the experiment and the solution from the Euler-equation solver (refer to Fig. 4a) with a period suggested by the experiment [6]. The hybrid simulation can then stably produce an unsteady flow field, in which the shock wave oscillates between the numerically predicted position and the measured position (see Figs. 4b and 4c). Although such a synthetic surface pressure field is not physically meaningful, this test suggests that the hybrid simulation can incorporate unsteady PSP data. In the presentation, we discuss details of the implementation of the Dirichlet boundary condition on the wall surface as well as the limitations and the potential issues of this PSP-driven hybrid simulation.

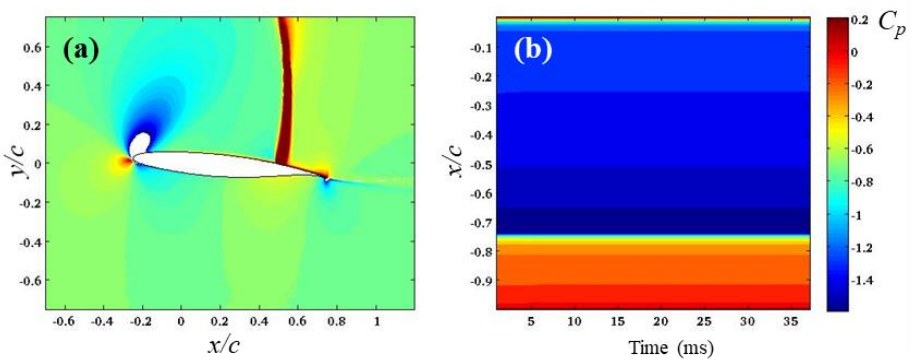

Fig. 3 *First-order Euler-equation solution for NASA CRM65 at $\alpha = 6^o$. (a) Density gradient. (b) Cp profile over time.*

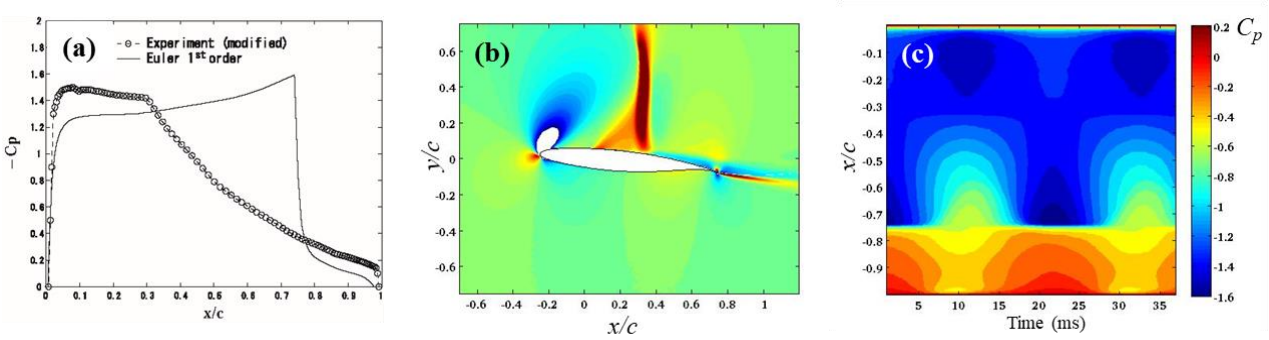

Fig. 4 *Application of the PSP-drive unsteady hybrid simulation for NASA CRM65 at $\alpha = 6^o$. (a) Comparison of Cp profiles, which are used for the synthetic Cp profile. (b) Density gradient of the hybrid simulation at the phase close to the experimental Cp profile (1st-order solver). (c) Cp profile over time produced by the hybrid simulation.*

References

[1] Suzuki T, Ji H, Yamamoto F (2006) Unsteady CFD velocity field solved with DNS. AIAA-2006-3450.
[2] Yamagata T, Hayase T, Higuchi H (2008) Effect of feedback data rate in PIV measurement-integrated simulation. J. Fluid Sci. Technol. 3: 477-487.
[3] Suzuki T, Chatellier L, Jeon Y J, David L (2018) Unsteady pressure estimation and compensation capabilities of the hybrid simulation combining PIV and DNS. Meas. Sci. Technol. 29: 125305 (15pp).
[4] Nisugi K, Hayase T, Shirai A (2004) Fundamental study of hybrid wind tunnel integrating numerical simulation and experiment in analysis of flow field. JSME Int. J. Ser. B 47(3): 593–604.
[5] Neeteson N J, Rival D (2017) Assimilation of surface pressure measurements into RANS simulation of a NACA0012 delta wing. 2nd workshop on Data Assimilation & CFD Processing for PIV and Lagrangian Particle Tracking, Delft, The Netherlands.
[6] Sugioka Y, Numata D, Asai K, Koike S, Nakakita K, Nakajima T (2018) Polymer/Ceramic pressure-sensitive paint with reduced roughness for unsteady measurement in transonic flow. AIAA J. 56(6): 2145-2156.
[7] Pulliam T H, Barton J T (1985) Euler computations of AGARD working group 07 airfoil test cases. AIAA-1985-0018.

3rd Workshop and Challenge on Data Assimilation & CFD Processing for PIV and LPT
November 19-20, 2020, virtual online meeting

State Observer data assimilation for RANS with time-averaged 3D-PIV data

Edoardo Saredi[1*], Andrea Sciacchitano[1] and Fulvio Scarano[1]
[1]TU Delft, Faculty of Aerospace Engineering, Delft, The Netherlands
* e.saredi@tudelft.nl

Abstract

This work proposes a direct integration of experimental data within low-fidelity CFD simulations to enhance the accuracy of the latter. The computational cost of high-fidelity simulations (i.e. LES, DNS), remains relatively high for their use in optimization studies, especially for high Reynolds number flows. As a result, CFD analysis makes most often use of the simplified approach offered by the Reynolds-averaged Navier-Stokes (RANS) formulation (Ferziger and Perić, 2002; Argyropoulos and Markatos, 2015). Considered to be the workhorse in aerodynamic engineering for many years to come (Xiao and Cinnella, 2019), RANS solvers model the entire turbulent spectrum, achieving lower computational cost and higher robustness with respect to mentioned higher fidelity models. The cost of the amount of required modelling is the aforementioned lower accuracy (Davidson and Peng, 2003). In order to enhance the accuracy of low-fidelity simulation, several data assimilation (DA) methodologies have been presented in the literature. Among them, three main categories have emerged: variational methods (Foures et al., 2014; among others), Kalman filter (KF; Kalman, 1960; Kato et al., 2015) and state observer methods (reviewed in Hayase, 2015). In this work, the application of a state observer algorithm as data assimilation technique for a steady RANS simulation is investigated. The concept of state observers, introduced by Luenberger (1964), is nowadays a key concept in the field of control theory. In this framework, the state observer refers to the insertion of a momentum source **f** in the momentum equation as follows:

$$(\bar{\mathbf{u}} \cdot \nabla)\bar{\mathbf{u}} = -\nabla\bar{p} + \nu\Delta\bar{\mathbf{u}} - \nabla \cdot \mathbf{R} + \mathbf{f}$$

where **R** represents the Reynolds stress tensor. The relative strength of the body force term represents the feedback and it is proportional to the local difference between the simulation and the experimental time-averaged velocities ($\mathbf{u}^*_{\mathrm{ref}}$), that reads $\mathbf{e} = (\mathbf{u}^*_{\mathrm{ref}} - \mathbf{u})$. In this work, two different forms of the feedback term have been considered: data assimilation based on state observer i) with proportional feedback (DASOP), and ii) with proportional-integral feedback (DASOPI). The feedback control law used in the DASOP method is given by $\mathbf{f_{DASOP}} = \frac{K_p}{D}\mathbf{e} \circ |\mathbf{e}|$, where K_p is the proportional feedback gain, the symbol $\circ$ represents the Hadamard product and $|\mathbf{e}|$ is the component-wise absolute value of the error $|\mathbf{e}| = [|\mathrm{e_x}|, |\mathrm{e_y}|, |\mathrm{e_z}|]^T$. The forcing term for the DASOPI method is given by $\mathbf{f_{DASOPI}} = \frac{K_p}{D}\mathbf{e} \circ |\mathbf{e}| + \frac{\mathrm{K_i}}{\mathrm{D}}\sum_{n=1}^{N}\mathbf{e}_{\mathrm{n}} \circ |\mathbf{e}_{\mathrm{n}}|$, where N is the current iteration and K_i is the integral feedback gain and $\mathbf{e}_{\mathrm{n}}$ is the local error vector at the iteration n. The gains K_p and K_i are scalars as they are assumed equal for each component of the error and constant along the simulation and spatially in the entire simulation domain. The values corresponding to cells where $\mathbf{u}^*_{\mathrm{ref}}$ is not available are set to 0, thus disabling the forcing term. This technique is demonstrated on an experimental database that describes the time-average three-dimensional flow behind a generic car-mirror model, formed by half a cylinder with a quarter of a sphere mounted above it. The experiment is run at the TU Delft High Speed Laboratory, in an open-jet low-speed wind tunnel (W-tunnel). The experimental setup is shown in Fig. 1 (left). The Reynolds number is $\mathrm{Re_D} = 8 \times 10^4$, obtained by considering a free-stream velocity $U_\infty = 12$ m/s and a base diameter equal to $D = 10$ cm.

The velocity field is obtained by means of Robotic Volumetric PIV measurements (Jux et al., 2018). The instantaneous particle positions and velocities obtained by the particle tracking algorithm *Shake-The-Box* (STB) implemented in the LaVision software *DaVis 10* are then ensembled averaged. Through this operation, a grid of 151 x 84 x 69 data points is obtained, which represents $\mathbf{u}^*_{\mathrm{ref}}$.

Once obtained the time-average flow field $\mathbf{u}^*_{\mathrm{ref}}$ from the experiment, the effects of the different forcing terms and the spatial density of the measurement input to the numerical simulation are studied.

All the numerical simulations have been performed with the open-source C++ toolbox *OpenFoam 1706*. For the baseline simulation, the one with no forcing applied, the standard steady solver *simpleFoam* implemented in *OpenFoam* is used.

For the assimilated simulations, the feedback term is included within an in-house developed version of the same solver. Turbulence modelling is based on the k-ω SST model.

For what concerns the spatial density of the forcing points, the normalised mean distance between neighbouring forcing cells $\gamma = \lambda/D$ has been varied, where $\lambda = \sqrt[3]{\frac{4}{3\pi C}}$ and $C = N_f/V$, with N_f equal to the number of forced cells, selected randomly, and V the total forced volume. The state observer approach forces locally the solution to comply with the reference value and the extent of the region modified by the forcing input is discussed. The velocity distribution and flow topology obtained with data assimilation are compared with attention to the object wake and the reattachment point where the largest discrepancy is observed between the different approaches. Fig. 1 (right) shows the behaviour of $\bar{\varepsilon}$, the spatial average of the normalized error between the reference data and the simulations in the forced volume, at different values of γ. The results show that both DASOP and DASOPI are able to diminish the distance between the simulation and the reference. The addition of the integral term allows to obtain a lower mismatch between simulation and the reference data, with increasing benefits when the distance between forced points is reduced.

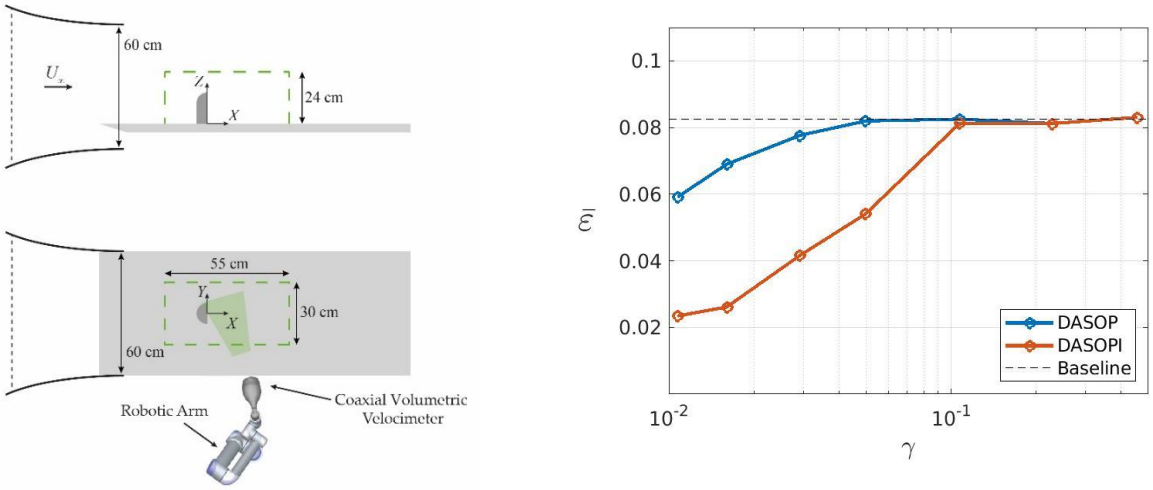

Fig. 1 Setup of the experiment (left) and spatial-averaged relative error $\bar{\varepsilon}$ with respect to the relative mean force point distance γ (right).

References

Argyropoulos CD and Markatos NC (2015) Recent advances on the numerical modelling of turbulent flows. Appl Math Model 39: 693-732

Davidson L and Peng SH (2003) Hybrid LES-RANS modelling: a one-equation SGS model combined with a k–w model for predicting recirculating flows. Int J Numer Meth Fluids 43:1003-1018

Duraisamy K, Iaccarino G and Xiao H (2018) Turbulence Modeling in the Age of Data. Annu Rev Fluid Mech 51:1–23

Ferziger JH, Peric M (2002) Computational Methods for Fluid Dynamics. Springer-Verlag Berlin Heidelberg

Foures DPG, Dovetta N, Sipp D and Schmid PJ (2014) A data-assimilation method for Reynolds-averaged Navier–Stokes-driven mean flow reconstruction. J Fluid Mech 759:404-431

Hayase T (2015) Numerical simulation of real-world flows. Fluid Dyn Res 47:051201

Jux C, Sciacchitano A, Sciacchitano A and Scarano F (2020) Flow pressure evaluation on generic surfaces by robotic volumetric PIV. Meas Sci Tech 109645

Kalman RE (1960) A new approach to linear filtering and prediction problems. Trans ASME: J Basic Eng 82D:35-45

Kato H, Yoshizawa A, Ueno G and Obayashi S (2015) A data assimilation methodology for reconstructing turbulent flows around aircraft. J Comput Phys 283:559-581

Luenberger DG (1964) Observing state of linear system. IEEE Trans Mil Electron Mil8:74–80

Ronch AD, Panzeri M, Drofelnik J and d'Ippolito R (2019) Sensitivity and calibration of turbulence model in the presence of epistemic uncertainties. CEAS Aeronaut J

Xiao H and Cinnella P (2019) Quantification of model uncertainty in RANS simulations: A review. Prog Aerosp Sci 108:1-31

3rd Workshop and Challenge on Data Assimilation & CFD Processing for PIV and LPT
November 19-20, 2020, virtual online meeting

Enhanced mean flow reconstruction from punctual measurements through optimal sensor placement

Vincent Mons[1], Olivier Marquet[1] and Benjamin Leclaire[1]
[1]ONERA-DAAA, 8 rue des Vertugadins, 92190 Meudon, France
vincent.mons@onera.fr

Abstract

Flow reconstruction by data assimilation from measurements can aim at determining unresolved temporal or spatial scales, but also at extrapolating information to zones where measurements are unavailable or inaccurate. In both respects, a legitimate question for the experimentalist, which is still open to date, is whether performing the measurements at certain points of the flow (in the case of pointwise sensors), or in certain zones (e.g. in the case of PIV/LPT), might lead to better reconstructions than when choosing the locations traditionally, i.e. mostly based on physical knowledge and intuition. Our aim in the present contribution is to address this question, taking as objective the mean flow reconstruction, and starting from the case of pointwise measurements. The adopted formalism is in fact versatile, and will be straightforwardly extended to field measurements such as PIV or LPT in future steps. It firstly involves adjoint-based data assimilation to retrieve the full mean flow from punctual mean velocity measurements. Sensor placement methodologies are then developed to determine optimal locations for these punctual measurements in order to maximize the reconstruction performances of data assimilation.

To perform the reconstruction of a full mean flow from punctual mean velocity measurements, we here rely on the adjoint-based data assimilation procedure proposed by Foures et al. (2014). The latter consists in determining the (supposedly unknown) divergence of the Reynolds stresses in the Reynolds-averaged Navier-Stokes (RANS) equations minimizing the discrepancies between the corresponding mean flow and the available measurements. Mathematically, this can be expressed as:

$$\min_{\boldsymbol{f}} \left\{ J = \frac{1}{2} \|\boldsymbol{y} - \boldsymbol{h}(\boldsymbol{u}, p)\|^2 \right\}$$

under the constraint

$$\nabla \cdot \boldsymbol{u} = 0$$
$$(\boldsymbol{u} \cdot \nabla \boldsymbol{u}) = -\frac{1}{\rho} \nabla p + \frac{1}{Re} \Delta \boldsymbol{u} + \boldsymbol{f}$$

In the above (RANS) mean flow equations for $\boldsymbol{u}$ and p, the optimized term $\boldsymbol{f}$, hereafter also termed forcing, indeed identifies to the divergence of the Reynolds stresses, i.e. $\boldsymbol{f} = -\nabla \cdot \overline{\boldsymbol{u}' \otimes \boldsymbol{u}'}$. In the objective functional J, $\boldsymbol{y}$ and $\boldsymbol{h}$ respectively denote the measurements, gathered as a single vector, and the measurement operator, extracting the values of the numerical mean flow $(\boldsymbol{u}, p)$ at the sensor locations, possibly also modelling their spatial resolution. Figure 1 illustrates the mean flow around a circular cylinder at $Re = 150$ along with the corresponding forcing, which forms the ground truth flow to reconstruct in the present study.

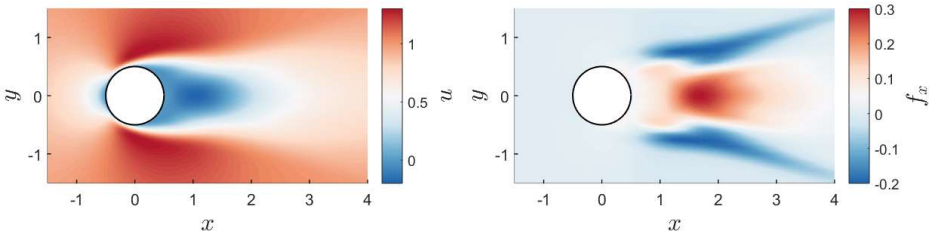

Fig. 1 Ground truth streamwise components of the mean velocity field (left) and associated forcing (right) for the flow around a circular cylinder at Re = 150.

The flow obtained with this data assimilation procedure and using a regularly spaced network of (synthetic) velocity sensors is illustrated in figure 2 (left column). Discrepancies with respect to the true mean flow are clearly identifiable, both outside and in the wake. Besides, the retrieved forcing appears significantly different from the true one (shown in Figure 1).

In order to improve these reconstruction results, we propose to minimize the condition number of the Hessian matrix (defined as the ratio between its largest and smallest eigenvalues) which is associated to the cost function in the data assimilation problem. This amounts to enhance the observability of changes in the control vector of the data assimilation problem (Kang and Xu, 2012), namely here the forcing $\boldsymbol{f}$ in the RANS equations. A difficulty here is the nonlinearity of the RANS equations, which makes the spectrum of this Hessian matrix vary with the forcing. This is solved through the development of the second-order adjoint model (Le Dimet et al, 2002) for the RANS equations, which allows designing an efficient optimization procedure to minimize the condition number of the Hessian.

Starting from the regularly spaced sensors, the application of this optimization procedure for sensor placement allows designing the network that is illustrated in figure 2 (right column). The mean flow obtained through data assimilation relying on these optimized sensors appears significantly closer to the true one compared to the use of the first-guess sensors, with vanishing discrepancies in the wake. The reconstructed forcing is also closer to the true divergence of the Reynolds stress tensor.

This numerical experiment confirms the validity of the proposed sensor placement methodology. Future work will be dedicated to its extension to the reconstruction of higher Reynolds number, turbulent flows, the design of an actual experiment, and to the optimization of other types of measurements, including field measurement (e.g. choice of the location of PIV/LPT planes/volumes when reconstructing large flow volumes which cannot be completely measured).

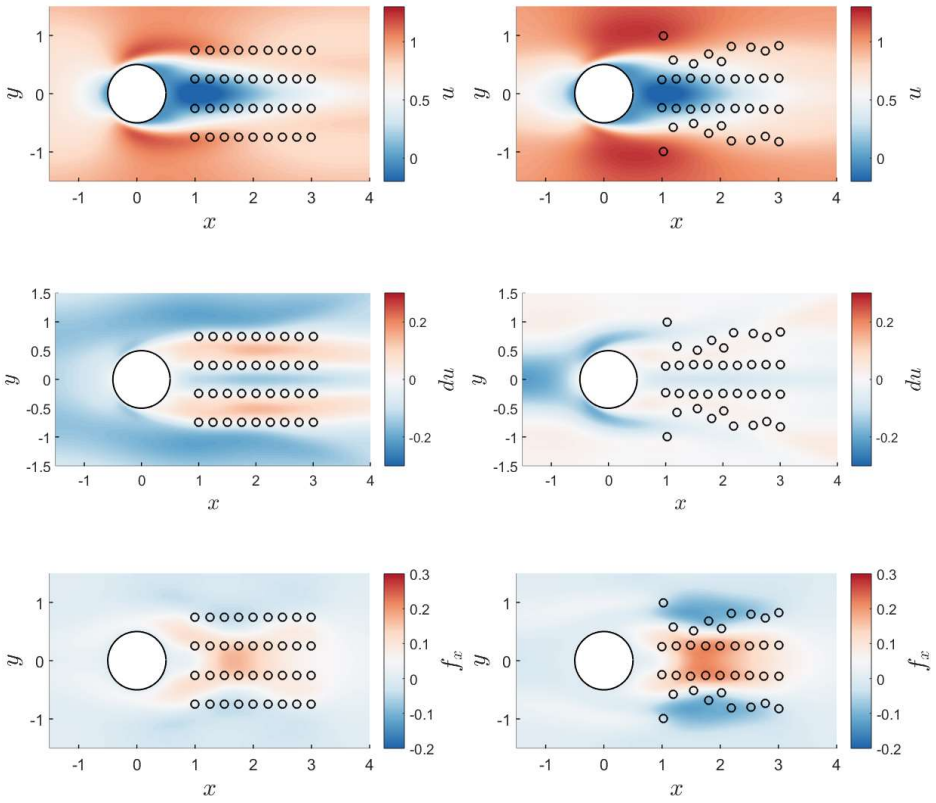

Fig. 2 Reconstructed flow relying either on first-guess sensors (left column) or on optimized sensors (right column). First to third rows respectively report the streamwise component of the reconstructed mean flow, its difference with the ground truth, and the streamwise component of the reconstructed forcing, respectively.

References

Foures D P G, Dovetta N, Sipp D, Schmid P J (2014) A data-assimilation method for Reynolds-averaged Navier-Stokes-driven mean flow reconstruction. Journal of Fluid Mechanics. 759:404-431. doi:10.1017/jfm.2014.566

Kang W, Xu, L. (2012) Optimal placement of mobile sensors for data assimilations. Tellus A. 64:17133. doi:10.3402/tellusa.v64i0.17133

Le Dimet, F-X, Navon I M, Daescu, D N (2002) Second-order information in data assimilation. Monthly Weather Review. 64:17133. doi:10.1175/1520-0493(2002)130<0629:SOIIDA>2.0.CO;2